https://doi.org/10.5194/essd-2022-308
Preprint. Discussion started: 20 September 2022

Open Access Earth System Science Data Discussions

GOBAI-O_2: temporally and spatially resolved fields of ocean interior dissolved oxygen over nearly two decades

Jonathan D. Sharp[1,2], Andrea J. Fassbender[2], Brendan R. Carter[1,2], Gregory C. Johnson[2], Cristina Schultz[3,4], John P. Dunne[3]

[1]Cooperative Institute for Climate, Ocean, and Ecosystem Studies, University of Washington, Seattle, WA, 98105, United States

[2]Pacific Marine Environmental Laboratory, National Oceanic and Atmospheric Administration, Seattle, WA, 98115, United States

[3]Geophysical Fluid Dynamics Laboratory, National Oceanic and Atmospheric Administration, Princeton, NJ, 08540, United States

[4]Princeton University, Princeton, NJ, 08540, United States

Correspondence to: Jonathan D. Sharp (jonathan.sharp@noaa.gov)

Abstract. Over a decade ago, oceanographers began installing oxygen sensors on Argo floats to be deployed throughout the world ocean with the express objective of better constraining trends and variability in the ocean's inventory of oxygen. Until now, measurements from these Argo-mounted oxygen sensors have been mainly used for localized process studies on air–sea oxygen exchange, biological pump efficiency, upper ocean primary production, and oxygen minimum zone dynamics. Here we present a four-dimensional gridded product of ocean interior oxygen, derived via machine learning algorithms trained on dissolved oxygen observations from Argo-mounted sensors and discrete measurements from ship-based surveys, and applied to temperature and salinity fields constructed from the global Argo array. The data product is called GOBAI-O_2 for Gridded Ocean Biogeochemistry from Artificial Intelligence – Oxygen (Sharp et al., 2022; https://doi.org/10.25921/z72m-yz67; last access: 30 Aug. 2022); it covers 86% of the global ocean area on a 1° latitude by 1° longitude grid, spans the years 2004–2021 with monthly resolution, and extends from the ocean surface to two kilometers in depth on 58 levels. Two machine learning algorithms — random forest regressions and feed-forward neural networks — are used in the development of GOBAI-O_2, and the performance of those algorithms is assessed using real observations and Earth system model output. GOBAI-O_2 is evaluated through comparisons to the World Ocean Atlas and to direct observations from large-scale hydrographic research cruises. Finally, potential uses for GOBAI-O_2 are demonstrated by presenting average oxygen fields on isobaric and isopycnal surfaces, average oxygen fields across vertical–meridional sections, climatological cycles of oxygen averaged over different pressure intervals, and a globally integrated oxygen inventory time series.

https://doi.org/10.5194/essd-2022-308
Preprint. Discussion started: 20 September 2022

1 Introduction

The inventory of dissolved oxygen in the global ocean has been declining over recent decades and is projected to continue to decline through the current century (Breitburg et al., 2018; Bindoff et al., 2019; Stramma and Schmidtko, 2019; Limburg et al., 2020), leading to detrimental consequences for aerobic marine organisms (Pörtner and Farrell, 2008; Sampaio et al., 2021) and changes to biogeochemical cycles, potentially triggering important climatological feedbacks (Gruber, 2004; Berman-Frank et al., 2008). Historical deoxygenation has been inferred from analyses of globally distributed observations (Helm et al., 2011; Schmidtko et al., 2017; Ito et al., 2017) and has been reproduced in Earth system model (ESM) reconstructions (Bopp et al., 2013; Frölicher et al., 2009; Kwiatkowski et al., 2020). Observational studies have generally indicated a greater degree of deoxygenation than model studies over recent decades, indicating that ESMs may misrepresent the sensitivities of the physical and biological processes leading to deoxygenation, which has implications for the reliability of future projections (Oschlies et al., 2017; 2018). On the other hand, model studies are based on gridded output that is continuously resolved in space and time, whereas observational studies rely on interpolation of discrete bottle measurements and/or measurements from CTD mounted sensors that have significant spatiotemporal gaps, calling into question the representativeness of observation-based global deoxygenation trends.

Discrete measurements of dissolved oxygen concentration ($[O_2]$) are typically made using Winkler titrations (Winkler, 1888; Carpenter, 1965; Langdon, 2010), which are also used to calibrate measurements from electrode (or more recently sometimes optical) dissolved oxygen sensors mounted on Conductivity-Temperature-Depth (CTD) profilers. Globally distributed $[O_2]$ observations from discrete measurements and CTD profilers have been provided by hydrographic programs like the World Ocean Circulation Experiment (WOCE), the Climate and Ocean: Variability, Predictability and Change (CLIVAR) program, and the Global Ocean Ship-Based Hydrographic Investigations Program (GO-SHIP). Data from these programs are publicly available and are conveniently compiled into databases such as the World Ocean Database (WOD; Boyer et al., 2018) and the Global Ocean Data Analysis Project (GLODAP; Lauvset et al., 2021). Though unprecedented spatial coverage is provided by global hydrographic programs, the decadal-scale temporal resolution of WOCE, CLIVAR, and GO-SHIP data prevents robust analyses of year-to-year and/or seasonal variability in $[O_2]$.

Since the mid-2000s, more than 1,600 Argo floats equipped with oxygen optodes have been deployed. Argo floats profile the upper ~2000 meters of the water column every ~10 days. Many oxygen-equipped Argo floats have been deployed as parts of regional arrays such as the Southern Ocean Carbon and Climate Observations and Modeling (SOCCOM; soccom.princeton.edu) project and the North Atlantic Aerosols and Marine Ecosystems Study (NAAMES; science.larc.nasa.gov/NAAMES/). More recently, the push for a global biogeochemical Argo array has spurred the deployment of oxygen-equipped Argo floats into more sparsely sampled ocean regions (Johnson and Claustre, 2016; Claustre et al., 2020). As more floats have been deployed, improvements have been made to sensor calibration, data adjustments, and quality control.

https://doi.org/10.5194/essd-2022-308
Preprint. Discussion started: 20 September 2022

Notably, pre-deployment drift corrections (D'Asaro and McNeil, 2013; Johnson et al., 2015; Bittig and Körtzinger, 2015; Bushinsky et al., 2016; Drucker and Riser, 2016; Nicholson and Feen, 2017), climatology-based calibrations (Takeshita et al., 2013), calibrations via in-air oxygen measurements (Körtzinger et al., 2005; Fiedler et al., 2013; Bittig and Körtzinger, 2015; Johnson et al., 2015; Bushinsky et al., 2016), post-deployment drift corrections (Johnson et al., 2017; Bittig et al., 2018a), and well-established procedures for delayed-mode quality control (Maurer et al., 2021) have substantially improved the accuracy and reproducibility of optode-based [O_2] measurements on Argo floats.

From the start, the Argo-Oxygen program (now oxygen is a measured variable under the Biogeochemical Argo program) intended to document ocean deoxygenation, predict and assess anoxic and hypoxic events, and determine seasonal to interannual changes in export production (Gruber et al., 2010). Until now, these goals have been achieved primarily on a regional scale. For example, [O_2] measurements from biogeochemical Argo floats have been used to examine ventilation and air–sea exchange of oxygen in the Southern Ocean (Bushinsky et al., 2017) and during Deep Water formation in the Subpolar North Atlantic (Körtzinger et al., 2004; Piron et al., 2016; 2017; Wolf et al., 2018); denitrification and the spatial extent of the oxygen minimum zone in the Bay of Bengal (Sarma and Udaya Bhaskar, 2018; Johnson et al., 2019; Udaya Bhaskar et al., 2021); and carbon production and export in the Pacific Ocean (Bushinsky and Emerson, 2015, 2018; Yang et al., 2017), Southern Ocean (Stukel and Ducklow, 2017; Arteaga et al., 2019), and North Atlantic Ocean (Alkire at al., 2012; Estapa et al., 2019). Recently, Johnson and Bif (2021) used the diel cycle of oxygen measured by the ocean-wide array of biogeochemical Argo floats to constrain net primary production in the surface ocean, in an early global-scale analysis of [O_2] from the Argo array.

With this work, we seek to capitalize on the combined efforts of global hydrographic programs and the Biogeochemical Argo program to create a first-of-its-kind data product: a four-dimensional monthly record of dissolved oxygen in the global ocean. We combine autonomous observations of [O_2] from BGC Argo floats with discrete observations of [O_2] from hydrographic cruises in the GLODAP database to compile a dataset with extensive spatial and temporal resolution. With this dataset, we train machine learning (ML) algorithms, evaluate those algorithms, and apply the algorithms to ocean interior predictor variables to produce a gridded [O_2] data product at a monthly resolution from 2004–2021, on 58 pressure levels in the upper two kilometers of the ocean, and on a global 1° latitude by 1° longitude grid.

In this paper, we present the four-dimensional gridded [O_2] product — which we call GOBAI-O_2 (Gridded Ocean Biogeochemistry from Artificial Intelligence – Oxygen; Sharp et al., 2022; https://doi.org/10.25921/z72m-yz67; last access: 30 Aug. 2022) — analyzing spatial patterns, seasonal cycles, and decadal variability. We discuss the process for creating GOBAI-O_2, show the results of evaluation exercises, assess uncertainty in the gridded [O_2] fields, and compare the data product to other gridded datasets and discrete measurements. GOBAI-O_2 represents the first step in leveraging the emerging global array of BGC Argo floats to produce spatially-resolved, time-varying snapshots of global ocean biogeochemical distributions.

https://doi.org/10.5194/essd-2022-308
Preprint. Discussion started: 20 September 2022

Critically, GOBAI-O_2 can be used to address the goals of the Argo-Oxygen program set by Gruber et al. (2010) over a decade ago, providing insight into ocean deoxygenation and hypoxia on timescales ranging from a few months to multiple years.

2 Methods

2.1 Data sources and processing

Hydrographic cruise data were obtained from the GLODAP version 2021 data product (GLODAPv2.2021; Lauvset et al., 2021). GLODAPv2.2021 provides quality-controlled data from throughout the entire water column obtained via discrete analyses of more than 1.3 million water samples collected on 989 research cruises. Dissolved oxygen is the most represented biogeochemical variable in GLODAPv2.2021, with nearly 1.2 million data points from 905 research cruises. Data from GLODAPv2.2021 were filtered to retain only samples collected after 1 Jan. 2004, from 0 to 2050 decibars (dbars), and with quality control flags of 1 (meaning the data were manually inspected) and quality flags of 2 ("good") for salinity and [O_2]. Temperature is not assigned either flag and is assumed to be "good" if it exists (Lauvset et al., 2021). This left 410,079 data points from 20,625 unique profiles from 358 total cruises (red points in Fig. 1).

Float data were obtained from synthetic profile ("Sprof") files (Bittig et al., 2022) stored in the Argo Global Data Assembly Centres (GDACs) via the OneArgo-Mat toolbox (Frenzel et al., 2022) for MATLAB (MathWorks). At the time data were obtained, the Argo GDACs contained data from 1,616 floats equipped with [O_2] sensors. Float data were filtered to retain only delayed-mode-adjusted data with quality flags of 1 or 2 ("good" or "probably good") for pressure, temperature, salinity, and [O_2]. This filtering ensured float data had been manually reviewed by a data manager and assigned an appropriate quality flag. This left 13,300,840 data points from 117,342 unique profiles from 880 total floats (blue points in Fig. 1). A figure in the supplemental material (Fig. A1) displays the number of profiles made within each 1° x 1° box by either a discrete ship cast or Argo float, providing an idea of the temporal resolution of data in addition to the spatial distribution shown in Fig. 1.

Float-based and ship-based data used in algorithm training were grouped into seven overlapping regions (Fig. 1, Table B1). This grouping was intended to account implicitly for similar physical–biogeochemical relationships within large ocean regions and to reduce the computational burden of the machine learning (ML) algorithm fits described below. The regions were initially chosen to imitate the biomes presented by Fay and McKinley (2014), and were then expanded to relatively large regions bound either by land masses or by overlapping boundaries along constant lines of latitude.

Gridded temperature and salinity data to which the trained algorithms were applied were obtained from the latest version of the Roemmich and Gilson (2009) (RG09) Argo Climatology (https://sio-argo.ucsd.edu/RG_Climatology.html; last access: 19 Jan. 2022). The RG09 climatology is an upper ocean (0–2000 dbar) gridded temperature and salinity product constructed exclusively from Argo observations. Long-term (2004–2018) mean fields of temperature and salinity are provided on 58 depth

https://doi.org/10.5194/essd-2022-308
Preprint. Discussion started: 20 September 2022

levels, along with monthly anomaly fields on each of those depth levels from 2004 to the present day. The most recent major update of the RG09 climatology was made in 2019, and new monthly anomaly fields are provided in near-real-time between major updates. Monthly gridded temperature and salinity were calculated from the RG09 long-term mean and monthly anomaly fields (Fig. A2), then used for the creation of the gridded [O_2] product discussed below.

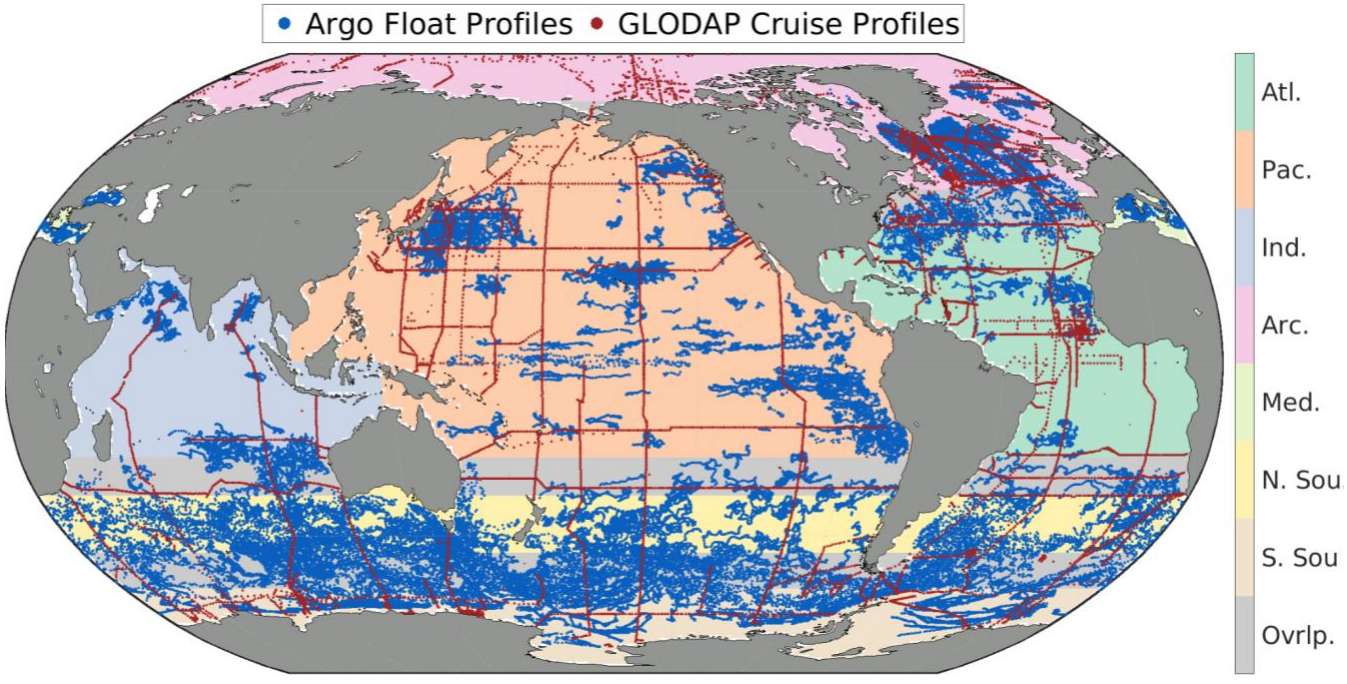

Figure 1: Profile locations from oxygen-equipped Argo floats (blue) and GLODAPv2.2021 cruises (red) from 1 Jan. 2004 to 1 Apr. 2022. Data from these profiles were used to train ML algorithms to estimate [O_2] in each of seven regions: the Atlantic Ocean (Atl.), Pacific Ocean (Pac.), Indian Ocean (Ind.), Arctic Ocean (Arc.), Mediterranean Sea (Med.), northern section of the Southern Ocean (N. Sou.), and southern section of the Southern Ocean (S. Sou.). Overlapping areas between regions are shown in grey (Ovrlp.), where [O_2] estimates are made by taking weighted averages of outputs from two overlapping regional ML schemes. The regional boundaries are presented in numerical form in Table B1.

Output from the NOAA Geophysical Fluid Dynamics Laboratory's Earth System Model Version 4 (GFDL-ESM4; Dunne et al., 2020) was used to assess algorithm performance. Model output was downloaded from the World Climate Research Programme database (https://esgf-node.llnl.gov/projects/cmip6/; last access: 8 Apr. 2022), which hosts data from models participating in the sixth phase of the Coupled Model Intercomparison Project (CMIP6). Potential temperature, practical salinity, and [O_2] were downloaded to coincide with available ocean interior observations (Fig. A3). Historical outputs (2004–2014) and projected outputs under SSP2-4.5 (2015–2021) were combined to cover the time period over which observations were available. A spatial mask was applied to retain only GFDL-ESM4 grid cells with corresponding temperature and salinity values in the RG09 climatology, because that is the final grid on which GOBAI-O_2 is produced.

https://doi.org/10.5194/essd-2022-308
Preprint. Discussion started: 20 September 2022

2.2 Algorithm training

A combined dataset of GLODAP cruise-based and Argo float-based data was used to train ML algorithms to estimate [O_2] from absolute salinity, conservative temperature, potential density anomaly, pressure, bottom depth, and additional spatiotemporal information to allow for geographic, seasonal, and interannual variation (see Table 1). Though biology is not explicitly accounted for in the ML algorithms, Giglio et al. (2018) demonstrate that inclusion of spatiotemporal variables can implicitly accommodate biological processes with an appropriately distributed dataset.

Absolute salinity (S_A) was calculated from practical salinity (S_P), hydrostatic pressure (P), latitude, and longitude. Conservative temperature (T_{CNS}) was calculated from in situ temperature (T), S_A, and P. Potential density anomaly (σ_θ) was calculated from S_A and T_{CNS}. These calculations were made using the Gibbs-SeaWater (GSW) Oceanographic Toolbox for MATLAB (McDougall and Barker, 2011). As was done by Carter et al. (2021), longitude was transformed into two separate predictors: cos(Longitude − 20° E) and cos(Longitude − 110° E). Cosine functions were applied to maintain the cyclical nature of longitude as a predictor, and offsets of 20° E and 110° E were intended to shift regions where the cosine function has minimum explanatory power over landmasses. Bottom depth was determined by matching each observational location with the corresponding bathymetry from the ETOPO2v2 global relief model (NOAA National Geophysical Data Center, 2006).

Table 1. Predictor variables used to train random forest regressions and feed-forward neural networks.

Predictor Variable	Abbreviation	Unit	Range (approx.)
Conservative Temperature	T_{CNS}	°C	−2 to 32
Absolute Salinity	S_{ABS}	N/A	10 to 40
Potential Density Anomaly	σ_θ	kg m^{-3}	10 to 29
Hydrostatic Pressure	P	dbar	0 to 2000
Latitude	lat	°	−78 to 83
cos(Longitude – 20°)	lon_{cos20}	N/A	−1 to 1
cos(Longitude – 110°)	lon_{cos110}	N/A	−1 to 1
Bottom depth	bot	meters	0 to 10,000
Year	yr	years	2004 to 2022
sin(2π · Day of Year / 365.25)	doy_{sin}	N/A	−1 to 1
cos(2π · Day of Year / 365.25)	doy_{cos}	N/A	−1 to 1

Two types of ML algorithms were trained: feed-forward neural networks (FNNs; Demuth et al., 2008) and random forest regressions (RFRs; Breiman, 2001). Three separate FNNs were trained for each of the seven basins shown in Fig. 1, with an average of the three taken to obtain one equally weighted FNN result. The FNNs were constructed using the "feedforwardnet"

https://doi.org/10.5194/essd-2022-308
Preprint. Discussion started: 20 September 2022

function and trained using the "train" function, both from Version 14.4 of the Deep Learning Toolbox for MATLAB (R2022a). Each FNN was trained using a Levenberg-Marquardt algorithm, with 15% of the data reserved for testing the network during training steps. Each FNN had two hidden layers, with the following combinations of neurons in the first and second layer, respectively: 20 and 10, 15 and 15, and 10 and 20. One RFR was trained for each of the seven basins shown in Fig. 1. RFRs are ensembles of decision trees, each created with a bootstrapped version of the full dataset chosen randomly with replacement. Each RFR consisted of 400 trees, a minimum leaf size of 10, and six of the eleven predictors used for each decision split. These parameters were chosen after some trial and error to strike a balance between computational efficiency and algorithm performance. The MATLAB "treebagger" function was used to train RFRs.

In areas where two regions overlap (see Fig. 1), weighted averages of $[O_2]$ estimates were calculated in overlapping grid cells from each regional algorithm. These averages were weighted by distance from the center latitude line of the overlapping area (e.g., a point at 30 °S in the overlapping area between the N. Sou. region (whose northernmost border extends to 25 °S) and the Atl. region (whose northernmost border extends to 35 °S) would be calculated as $[O_2] = 0.5[O_2]_{N.Sou.} + 0.5[O_2]_{Atl.}$). Overlapping areas were used to mitigate discontinuities at the boundaries between regions in the final gridded product.

The average of FNN and RFR estimates (ENS, for ensemble average) was used as the $[O_2]$ estimate for a given set of input data. This ensemble averaging procedure was implemented due to insights from previous work showing that averaging the outputs of multiple ML algorithms or linear regression models often outperforms the output from just one approach on its own (Gregor et al., 2017; 2019; Bittig et al., 2018b; Carter et al., 2021; Djeutchouang et al., 2022), likely due to complementary strengths and weaknesses of each approach. For this work, any especially erroneous result from either the FNN or RFR should be mitigated by better results from the other algorithm.

2.3 Algorithm evaluation

Two exercises were performed to evaluate the effectiveness of the ML scheme used to estimate $[O_2]$. The first exercise involved training separate evaluation algorithms ($RFR_{Data\text{-}Eval}$ and $FNN_{Data\text{-}Eval}$ algorithms) as described in section 2.2 using a subset of the observational dataset for training while reserving the remaining subset for assessment. For this exercise, data were split randomly into training (80%) and assessment (20%) groups; this split was made according to measurement platform (cruise or float; see Fig. A4) to ensure that inherent correlations among the data points from a single cruise or float did not contribute to the apparent effectiveness of the ML scheme. $[O_2]$ values from the subset of reserved assessment data were compared to estimates of $[O_2]$ from $RFR_{Data\text{-}Eval}$, $FNN_{Data\text{-}Eval}$, and the ensemble average of the two ($ENS_{Data\text{-}Eval}$). This exercise was intended to evaluate the ability of the ML scheme to reproduce measured data that was not involved in algorithm training (section 3.1.1).

The second exercise involved training evaluation algorithms ($RFR_{ESM4\text{-}Eval}$ and $FNN_{ESM4\text{-}Eval}$ algorithms) using synthetic profiles extracted from GFDL-ESM4 output at the times and locations where observational data were available, then assessing

https://doi.org/10.5194/essd-2022-308
Preprint. Discussion started: 20 September 2022

the evaluation algorithms using spatially and temporally continuous monthly GFDL-ESM4 output from 2004 through 2021. For this exercise, synthetic profiles for algorithm training were defined by matching the latitude, longitude, month, and year of each available profile from the observational dataset with the nearest available GFDL-ESM4 output. As such, multiple profiles in the observational dataset could correspond to the same synthetic profile from GFDL-ESM4. This resulted in 68,242 synthetic profiles for algorithm training, compared to the 6,877,656 synthetic profiles available from the complete model output, which were used for assessment. $RFR_{ESM4\text{-}Eval}$ and $FNN_{ESM4\text{-}Eval}$ algorithms were trained as described in section 2.2 with the synthetic training data. Then, $[O_2]$ values from GFDL-ESM4 output were compared to estimates of $[O_2]$ from $RFR_{ESM4\text{-}Eval}$, $FNN_{ESM4\text{-}Eval}$, and an ensemble average of the two ($ENS_{ESM4\text{-}Eval}$). This exercise was intended to evaluate the ability of the ML scheme to estimate $[O_2]$ in a fully resolved Earth system model environment when limited to training data representative of the available collection of ocean oxygen observations (section 3.1.2).

The second exercise also resulted in a four-dimensional field of $[O_2]$ from $ENS_{ESM4\text{-}Eval}$ that represents a reconstruction of the GFDL-ESM4 environment. This field will be referred to as GOBAI-O_2-ESM4, and can be used as an analogue for how well GOBAI-O_2 (trained on real observational data, section 2.4) might represent the real-world environment. For this reason, the four-dimensional field of differences between GOBAI-O_2-ESM4 and GFDL-ESM4 output were used to inform the evaluation of GOBAI-O_2 uncertainty (sections 2.5 and 3.2.4).

2.4 Creation of GOBAI-O_2

FNNs and RFRs for each of the seven regions shown in Fig. 1 were trained with the full combined dataset of GLODAP and Argo data, using the predictor variables shown in Table 1 and $[O_2]$ as a target variable. Then, the FNNs and RFRs were applied to S_A, T_{CNS}, and σ_θ calculated from RG09 temperature and salinity fields, along with spatiotemporal information from RG09 grid cells. Ensemble averages (ENS) were calculated from the FNN and RFR estimates. This produced a monthly gridded $[O_2]$ product in the upper two kilometers of the ocean on a global grid from January 2004 to December 2021, i.e. GOBAI-O_2 (Sharp et al., 2022; https://doi.org/10.25921/z72m-yz67; last access: 30 Aug. 2022; sections 3.2.1–3.2.3). GOBAI-O_2 was compared to gridded climatological oxygen fields from the 2018 World Ocean Atlas (WOA18; Garcia et al., 2019; section 3.2.5) and to measurements of in situ oxygen from select cruises between 2004 and 2021 (section 3.2.6).

2.5 Uncertainty estimation

Similar to previous studies that have estimated uncertainty in observation-based biogeochemical data products (e.g., Landschützer et al., 2014; Gregor and Gruber, 2021; Keppler et al., 2020), we combine uncertainty from three separate sources — measurement, representation, and algorithm — to estimate uncertainty in GOBAI-O_2 (section 3.2.4).

Measurement uncertainty ($u([O_2])_{meas.}$) is attributable to the $[O_2]$ observations themselves. For this quantity, GOBAI-O_2 gridded $[O_2]$ is multiplied by 1.5%, which is between the nominal value for the consistency of the GLODAPv2.2021 cruise

https://doi.org/10.5194/essd-2022-308
Preprint. Discussion started: 20 September 2022

dataset — stated to be 1% (Lauvset et al., 2021) — and the approximate accuracy of BGC Argo float observations — estimated as about 3 μmol kg^{-1} (Johnson et al., 2017; Maurer et al., 2021), which is close to 2% of average ocean [O_2]. We recognize, however, that even 2% is a rather optimistic estimate for the accuracy of float [O_2] sensors, especially when crossing steep vertical gradients (Bittig and Körtzinger, 2017; Bittig et al., 2018). On a related note, no temporal lag corrections were applied to our float [O_2] dataset (Bittig et al., 2014; Bittig and Körtzinger, 2017).

Gridding uncertainty ($u([O_2])_{grid.}$) is attributable to using a single [O_2] value to represent a four-dimensional box that is coarser in time and space than the resolution of many processes that influence [O_2]. We estimate gridding uncertainty by (1) aggregating our combined GLODAP and Argo observational dataset to grid cells equal in size to the RG09 grid cells; (2) calculating the standard deviation among the observations in cells with more than ten observations (Fig. A5); (3) fitting a multivariate polynomial regression relating those standard deviations to depth, potential density anomaly, and distance from shore; and (4) applying that regression to the RG09 grid to calculate the expected standard deviation (i.e., gridding uncertainty) in each grid cell.

Algorithm uncertainty ($u([O_2])_{alg.}$) is attributable to the ML algorithms that estimate [O_2] on the RG09 grid. We estimate algorithm uncertainty using the four-dimensional field of absolute differences between [O_2] estimates from $ENS_{ESM4\text{-}Eval}$ versus [O_2] from GFDL-ESM4 model output, determined from the GFDL-ESM4 algorithm evaluation exercise described in section 2.3.

The three uncertainty sources were combined in quadrature (assuming independence) to calculate a combined uncertainty estimate for each gridded [O_2] value in GOBAI-O_2 ($u([O_2])_{tot.}$):

$$u([O_2])_{tot.} = \sqrt{u([O_2])^2_{meas.} + u([O_2])^2_{grid.} + u([O_2])^2_{alg.}} \quad (1)$$

3 Results and Discussion

3.1 Algorithm evaluation

The results of the evaluation exercises (Table 2) indicated that the ML algorithms trained on the combined GLODAP and Argo observational dataset were effective in their ability to estimate [O_2] from the set of predictor variables given in Table 1. Table 2 provides mean offsets (Δ[O_2]) and root mean squared differences (RMSDs) between [O_2] from direct measurements ($[O_2]_{obs}$) or GFDL-ESM4 output ($[O_2]_{mod}$) and [O_2] estimated from $ENS_{Data\text{-}Eval}$ or $ENS_{ESM4\text{-}Eval}$ algorithms ($[O_2]_{est}$); Tables B2 and B3 provide the same information for the RFR and FNN algorithms individually. Offsets are calculated as: $\Delta[O_2] = [O_2]_{obs/mod} -$

https://doi.org/10.5194/essd-2022-308
Preprint. Discussion started: 20 September 2022

$[O_2]_{est}$. In the case of the observational data-based validation test, mean $\Delta[O_2]$ and RMSD determined using $[O_2]_{est}$ from the ESPER-Mixed model (Carter et al., 2021) — an average of predictions from a neural network and moving window multiple linear regression trained on GLODAPv2.2020 data — are also shown. The results of each evaluation exercise are discussed in more detail in the following sections.

Table 2. Regional and global error statistics (mean $\Delta[O_2]$ and RMSD) for evaluation exercises using the ensemble average ($ENS_{Data\text{-}Eval}$) of $FNN_{Data\text{-}Eval}$ and $RFR_{Data\text{-}Eval}$ algorithms trained on a subset of data from the combined GLODAP and Argo observational dataset and tested with a separate subset of withheld data, or the ensemble average ($ENS_{ESM4\text{-}Eval}$) of $FNN_{ESM4\text{-}Eval}$ and $RFR_{ESM4\text{-}Eval}$ algorithms trained on a subset of output from GFDL-ESM4 (corresponding to locations of available Argo and GLODAP data) and tested using the full field of GDFL-ESM4 output. Error statistics calculated using the ESPER-Mixed model are also shown for comparison to the data-based test. The numbers of data points used in the training and assessment of each algorithm are shown.

Basin	Evaluation Exercise with Observational Data						Evaluation Exercise with GFDL-ESM4 Output			
	Training Data Points	Assessment Data Points	$ENS_{Data\text{-}Eval}$ Mean $\Delta[O_2]$	$ENS_{Data\text{-}Eval}$ RMSD	ESPER-Mixed Mean $\Delta[O_2]$	ESPER-Mixed RMSD	Training Data Points	Assessment Data Points	$ENS_{ESM4\text{-}Eval}$ Mean $\Delta[O_2]$	$ENS_{ESM4\text{-}Eval}$ RMSD
Atl.	358,316	249,549	-1.6	7.0	-5.2	10.9	161,122	26,720,928	-1.1	9.5
Pac.	2,318,956	534,670	-0.5	8.5	-3.2	11.2	473,330	65,746,512	0.2	8.5
Ind.	550,935	275,079	-0.5	5.6	-3.7	7.6	91,156	19,644,768	0.1	7.8
Arc.	809,258	314,004	-2.0	8.0	-0.2	10.9	231,582	10,939,968	-0.1	4.2
Med.	187,296	3,316	5.0	12.4	-2.5	14.4	31,330	1,038,960	1.7	5.8
N. Sou.	4,190,878	1,024,804	0.7	6.4	-0.4	9.3	701,636	64,067,328	0.0	4.3
S. Sou.	4,540,439	975,698	0.2	6.0	-0.2	8.1	488,176	29,759,184	0.0	3.3
Global	12,956,078	3,377,120	-0.3	6.9	-1.7	9.7	2,178,332	217,917,648	-0.1	7.2

3.1.1 Test with withheld observational data

Estimates of $[O_2]$ using $ENS_{Data\text{-}Eval}$ algorithms tracked closely with $[O_2]_{obs}$ and showed no strong systematic biases with $[O_2]_{est}$ or depth (Fig. 2a and 2b), though variability in $\Delta[O_2]$ was greatest near the surface. Mean offsets were between −2.0 and 5.0 μmol kg^{-1} for the seven regions, with a global average of −0.3 μmol kg^{-1}; RMSDs were between 5.6 and 12.4 μmol kg^{-1} for the seven regions, with a global average of 6.9 μmol kg^{-1} (Table 2). The slightly negative global average offset suggests somewhat higher estimated than measured $[O_2]$ values. The lowest RMSDs from the $ENS_{Data\text{-}Eval}$ algorithms were found in the Southern Ocean regions (Table 2 and Fig. 2c), likely due to the proliferation of float-based measurements from the SOCCOM program there (Fig. 1, Fig. A1, Fig. A4).

Estimates of $[O_2]$ using ESPER-Mixed (Fig. A6) showed average offsets between −5.2 and −0.2 μmol kg^{-1} for the seven regions (with a global average of −1.7 μmol kg^{-1}) and RMSDs between 7.6 and 14.4 μmol kg^{-1} for the seven basins (with a global average of 9.7 μmol kg^{-1}) (Table 2). Again, the negative global average offset suggests higher estimated than measured

https://doi.org/10.5194/essd-2022-308
Preprint. Discussion started: 20 September 2022

$[O_2]$ values. Compared to ESPER-Mixed (Carter et al., 2021), the $ENS_{Data\text{-}Eval}$ algorithms performed better, both in each individual region and overall. This result is likely a reflection of the fact that $ENS_{Data\text{-}Eval}$ algorithms were trained with more varied data than the ESPER-Mixed model (Argo and GLODAP compared to just GLODAP), and that the withheld data for which estimates were made also comprised more varied data (both Argo and GLODAP as well). Importantly, when estimates were made for just the GLODAP dataset, the $ENS_{Data\text{-}Eval}$ algorithms still performed better than ESPER-Mixed (Table B4), suggesting that the seasonally-resolved float data supply important information to the relationships established during algorithm training.

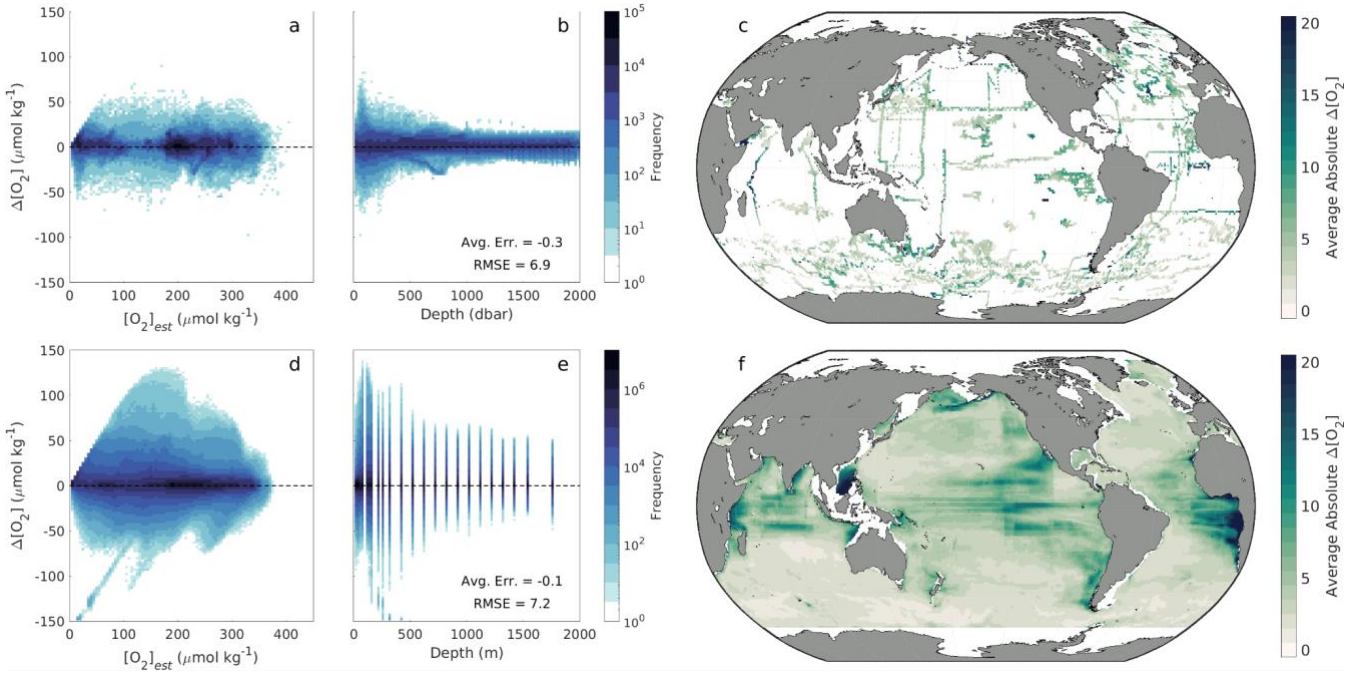

Figure 2. (a,b,d,e) Two-dimensional histograms showing offsets between measured versus estimated oxygen ($\Delta[O_2] = [O_2]_{obs} - [O_2]_{est}$) for withheld observational data (a,b) and modeled versus estimated oxygen ($\Delta[O_2] = [O_2]_{mod} - [O_2]_{est}$) for GFDL-ESM4 model output (d,e) as a function of $[O_2]_{est}$ (a,d) and depth in the water column (b,e). The frequency of offsets that fall into a given bin is shown on a logarithmic scale, emphasizing the clustering around $\Delta[O_2] = 0$. (c,f) Absolute $\Delta[O_2]$ values averaged over depth and time for 1° latitude by 1° longitude grid cells in the global ocean for withheld observational data (c) and GFDL-ESM4 model output (f).

3.1.2 Test with GFDL-ESM4 output

As introduced in section 2.3, the four-dimensional field of $[O_2]_{est}$ values calculated by applying $ENS_{ESM4\text{-}Eval}$ algorithms to GFDL-ESM4 output is referred to as GOBAI-O_2-ESM4. $[O_2]_{est}$ values from GOBAI-O_2-ESM4 tracked closely with $[O_2]_{mod}$ and showed no significant systematic biases with $[O_2]$ or depth (Fig. 2d and 2e). Similar to the data-based test, variability in

https://doi.org/10.5194/essd-2022-308
Preprint. Discussion started: 20 September 2022

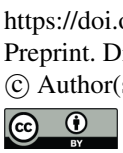

Open Access Earth System Science Data Discussions

$\Delta[O_2]$ was greatest near the surface. Average offsets were between −1.1 and 1.7 μmol kg^{-1} for the seven regions (with a global average of −0.1 μmol kg^{-1}) and RMSDs were between 3.3 and 9.5 μmol kg^{-1} for the seven basins (with a global average of 7.2 μmol kg^{-1}) (Table 2). The near-zero global average offset suggests that $[O_2]_{est}$ values from GOBAI-O_2-ESM4 matched well with values from GFDL-ESM4 output. The lowest RMSDs were found in the Southern Ocean regions (Table 2; Fig. 2f), again because these regions have the most available training data. One line of particularly low $\Delta[O_2]$ values (between about 0 and 100 μmol kg^{-1} in $[O_2]_{est}$ and 0 to 500 dbars in depth) is an indication of near-zero $[O_2]_{mod}$ and non-zero $[O_2]_{est}$, but does not appear to follow any coherent spatial pattern (analysis not shown) and is confirmed by the log-scaled frequency colorbar as a sporadic issue.

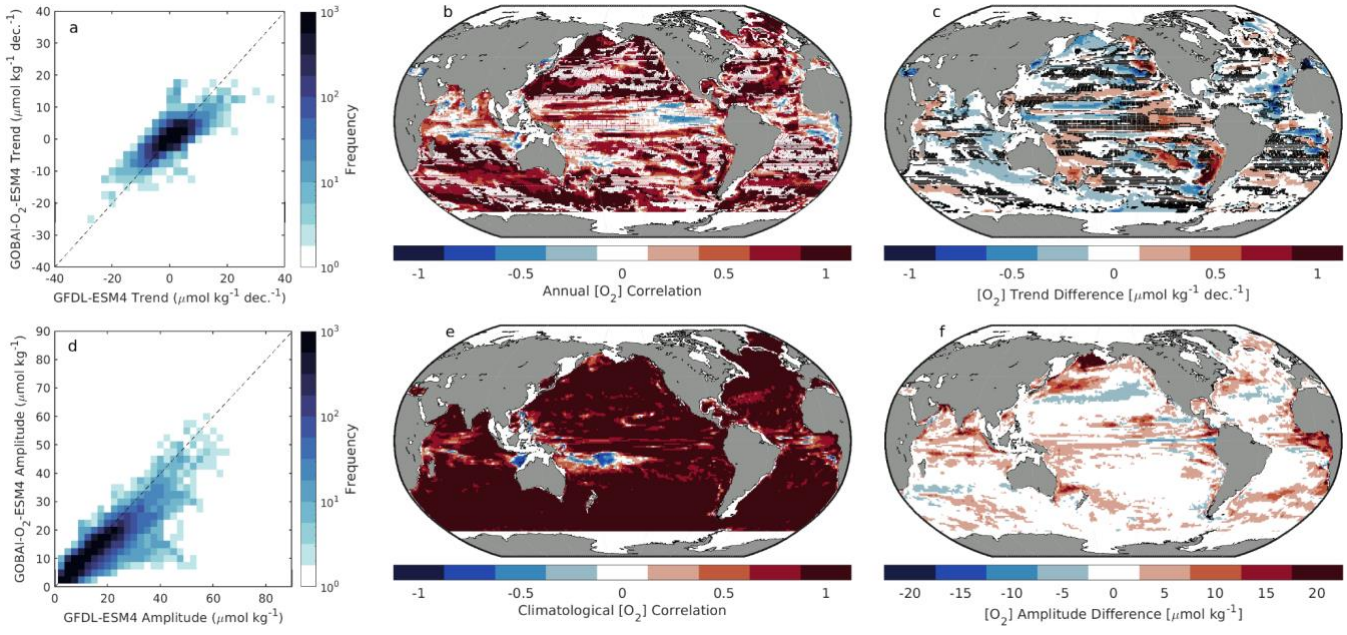

Figure 3. (a,d) Two-dimensional histograms showing grid cell level (a) trends in depth-weighted annual mean $[O_2]$ from 200 to 1000 dbars and (d) climatological amplitudes in depth-weighted monthly mean $[O_2]$ from 0 to 200 dbars between GFDL-ESM4 and GOBAI-O_2-ESM4. (b,e) Pearson's correlation coefficients between (b) depth-weighted annual mean $[O_2]$ from 200 to 1000 dbars, showing coherence between the subsurface trends, and (e) depth-weighted monthly mean $[O_2]$ from 0 to 200 dbars, showing coherence between the surface seasonal cycles. (c,f) Absolute difference between (c) trends in depth-weighted annual mean $[O_2]$ from 200 to 1000 dbars and (d) climatological amplitudes in depth-weighted monthly mean $[O_2]$ from 0 to 200 dbars between GFDL-ESM4 and GOBAI-O_2-ESM4.

GOBAI-O_2-ESM4 effectively captured the decadal scale and seasonal variability in the GFDL-ESM4 model environment (Fig. 3). The average Pearson's correlation coefficient between annual mean $[O_2]$ integrated from 200 to 1000 dbars from GFDL-ESM4 output versus GOBAI-O2-ESM4 was 0.66 ± 0.36 (Fig. 3a and 3b), and the trends differed in magnitude (GFDL-ESM4 minus GOBAI-O2-ESM4) by 0.0 ± 0.2 μmol kg^{-1} dec^{-1} (Fig. 3c). The average Pearson's correlation coefficient between monthly mean [O2] integrated from 0 to 200 dbars from GFDL-ESM4 output versus GOBAI-O_2-ESM4 was 0.91 ± 0.19 (Fig.

https://doi.org/10.5194/essd-2022-308
Preprint. Discussion started: 20 September 2022

3d and 3e), and the seasonal amplitudes differed in magnitude (GFDL-ESM4 minus GOBAI-O_2-ESM4) by 1.9 ± 4.2 μmol kg^{-1} (Fig. 3f). Absolute trends and seasonal amplitudes from each gridded field are shown in Fig. A7. When considered as a global average, the pattern in monthly mean [O_2] integrated from 200 to 1000 dbars matched well between GFDL-ESM4 output (−0.51 μmol kg–1 dec–1) and GOBAI-O_2-ESM4 (−0.59 μmol kg^{-1} dec^{-1}) (Fig. A8). Whether the internal variability in GFDL-ESM4 is truly representative of the ocean or is biased in one or more dimensions, the success of this evaluation exercise demonstrates an ability for the ML scheme employed here to capture that variability with the current distribution of available [O_2] observations as training data. This bodes well for the ability of GOBAI-O_2, which is trained on actual observational data, to represent decadal scale and seasonal variability in global ocean oxygen in the real world. However, it should be noted that the model output reflects meaningful spatial and temporal averaging and has no observational uncertainties, and thus the assessed skill can be thought of as an upper limit of the reconstruction skill achievable with the currently available observations.

The results of the exercise with GFDL-ESM4 model output are critical for evaluating the uncertainty of gridded oxygen values in GOBAI-O_2 (section 3.2.4). Further, the spatial distribution of Δ[O_2] (Fig. 2f) and the comparisons of reconstructed to modeled decadal trends and seasonal variability (Fig. 3b, 3c, 3e, 3f) can help inform our observing efforts (e.g., future cruise planning and BGC Argo float deployments). For example, large Δ[O_2] values in the eastern tropical Pacific and Atlantic, coupled with negative correlations in annual mean [O_2] and large differences in annual trends and seasonal amplitudes, suggest more observations will be required for GOBAI-O_2 to capture variability in that region.

3.2 GOBAI-O_2 product

3.2.1 Spatial oxygen distribution

The full GOBAI-O_2 product is available at https://doi.org/10.25921/z72m-yz67 (Sharp et al., 2022; last access: 30 Aug. 2022). Vertical–meridional sections of oxygen (Figs. 4 and 5) show that surface oxygen concentrations are generally high, as these waters tend to be near equilibrium with the atmosphere. This is particularly true at high latitudes where cold, dense waters have a high capacity for dissolved oxygen. Southern Ocean surface waters, however, are generally undersaturated with respect to oxygen (Fig. A9), confirming observations from previous studies that suggest this undersaturation is the result of O_2-depleted thermocline water upwelling into the mixed layer (Chierici et al., 2004; Reuer et al., 2007; Jonsson et al., 2013) making the Southern Ocean on average an oxygen sink (Gruber et al., 2001; Bushinsky et al., 2017). This phenomenon can also be observed in the equatorial Pacific (Fig. A9).

Iso-surface plots and vertical–meridional sections (Figs. 4 and 5) also reveal the signatures of distinct subsurface water masses. In each basin, well-ventilated subtropical mode waters can be identified by relatively high [O_2] at mid-latitudes on the 300 dbar surface (Fig. 4a) and along dips in isopycnals plotted against pressure and latitude (Fig. 4b–d) or along sloping isobars plotted against density and latitude (Fig. 5b–d) within the upper ~500 dbars. Beneath the southern mode waters in each basin,

https://doi.org/10.5194/essd-2022-308
Preprint. Discussion started: 20 September 2022

Antarctic Intermediate Water that originates in the Southern Ocean with a relatively high oxygen signal is prevalent. Beneath northern mode waters in the Pacific and Indian basins, respectively, relatively old and oxygen-poor North Pacific Intermediate Water (NPIW) and Red Sea Overflow Water (RSOW) can be observed (Talley et al., 2011). Beneath northern mode waters in the Atlantic, intermediate waters are younger and more highly oxygenated. Near the equator, subsurface oxygen minima are visible in each basin; this is a result of organic matter export from high production in the surface ocean that fuels strong subsurface respiration. Finally, the signatures of higher oxygen deep waters can be observed near the bottom of each vertical–meridional section.

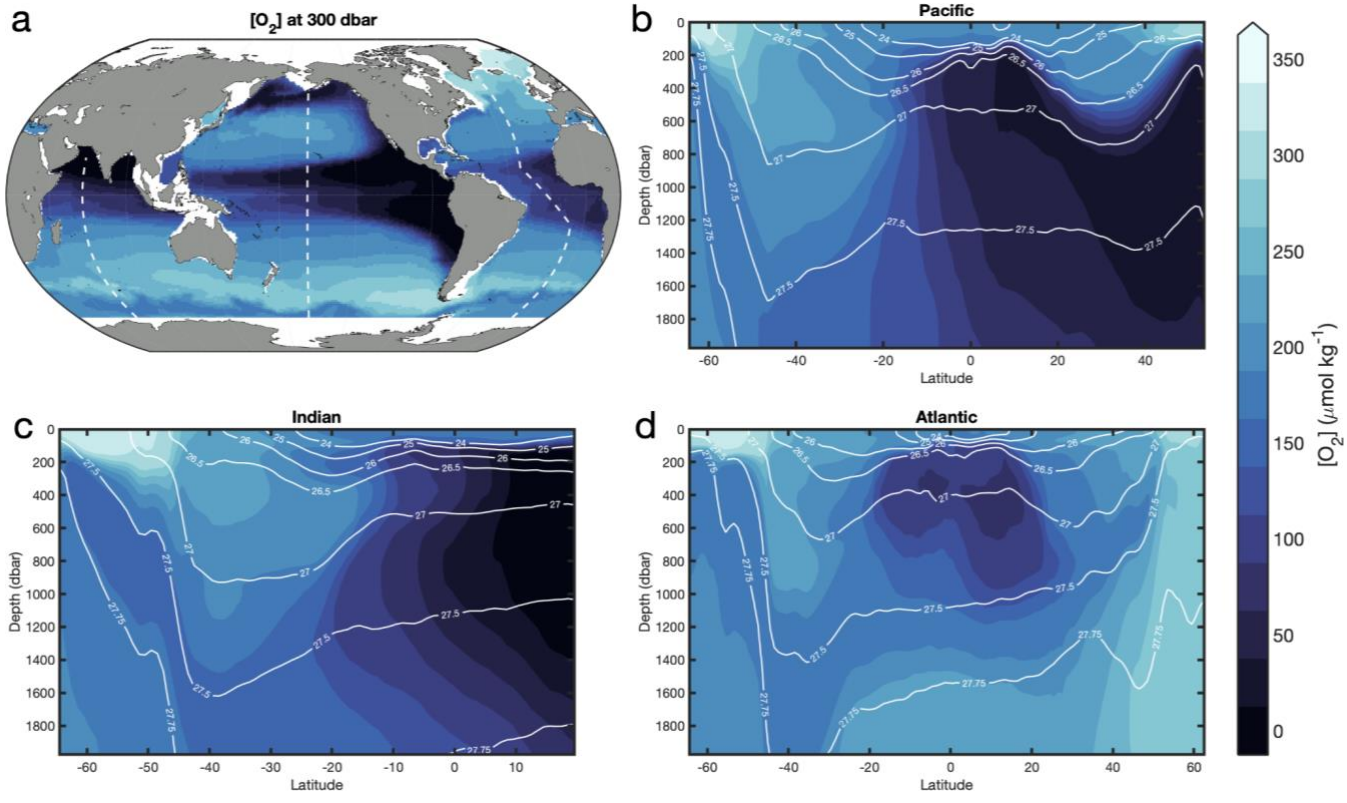

Figure 4. Long-term mean [O_2] from GOBAI-O_2 at 300 dbars (a) and from the surface to 2000 dbars in the Pacific (b), Indian (c), and Atlantic (d) Oceans. Dashed lines in panel a refer to the tracks of the sections in panels b–d. Contour lines in panels b–d are constant potential density surfaces (kg m^{-3}).

Oxygen concentrations at 300 dbars (Fig, 4a) are highest in the North Atlantic and Southern Oceans — where highly oxygenated, newly formed deep and intermediate waters are formed — and lowest in the North and Equatorial Pacific Ocean and the North Indian Ocean — where the oxygen content of subsurface waters has been greatly reduced by heterotrophic respiration. The same can be said for [O_2] on the 27 kg m^{-3} isopycnal (Fig. 5a). Oxygen concentrations are extremely low in the deep, high-density North Pacific Ocean and North Indian Ocean due to the ages of those water masses.

https://doi.org/10.5194/essd-2022-308
Preprint. Discussion started: 20 September 2022

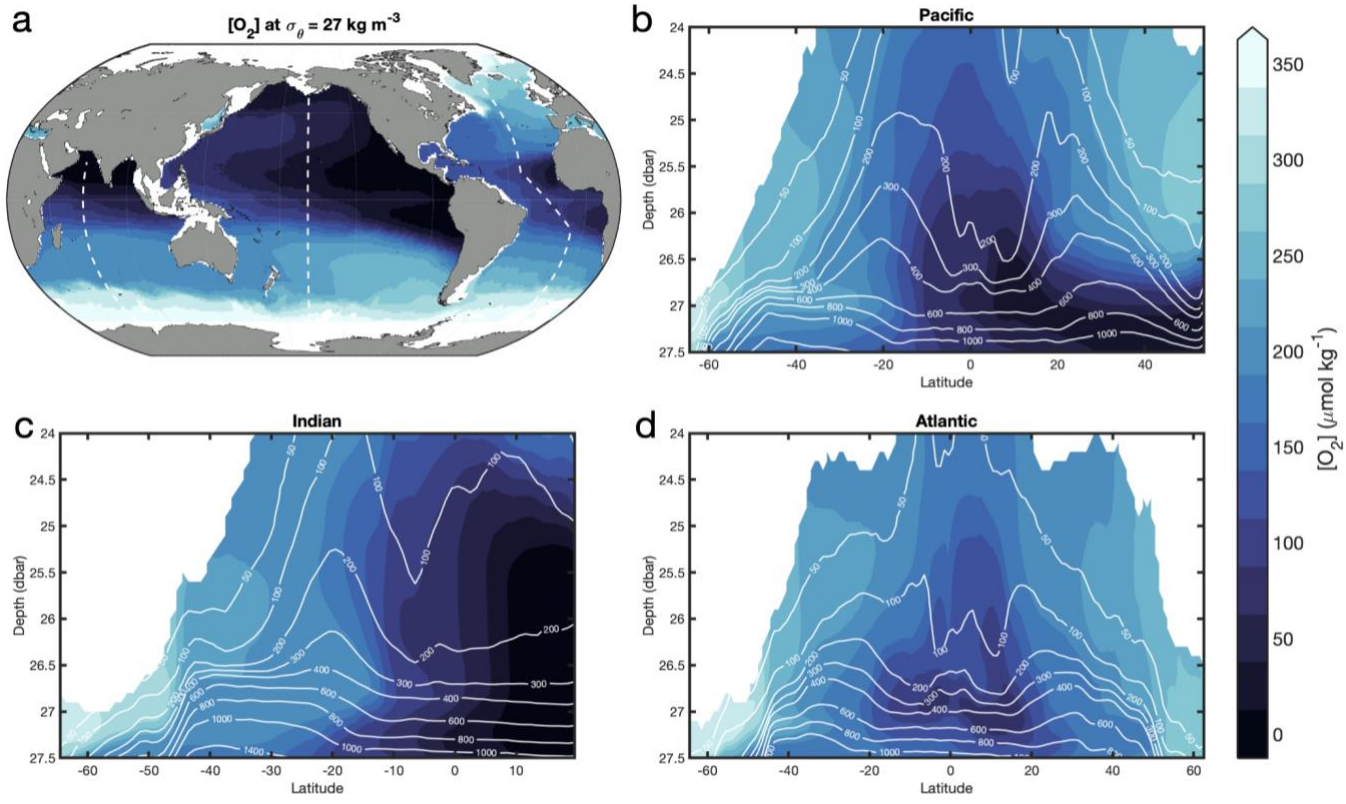

Figure 5. Long-term mean [O_2] from GOBAI-O_2 at σ_0 = 27 kg m^{-3} (a) and from σ_0 = 24 to 27.5 kg m^{-3} in the Pacific (b), Indian (c), and Atlantic (d) Oceans. Dashed lines in panel a refer to the tracks of the sections in panels b–d. Contour lines in panels b–d are constant pressure surfaces (dbars).

3.2.2 Climatological oxygen cycles

Climatological hemispheric mean [O_2] integrated over three pressure intervals (Fig. 6) reveals that the magnitude of the [O_2] seasonal cycle is greatest near the surface and decreases with depth. The amplitude of the [O_2] seasonal cycle in a near-surface interval (0–100 dbars) is about 8.4 μmol kg^{-1}. Maximum [O_2] in this interval (April/May in the Northern Hemisphere and October/November in the Southern Hemisphere) lags about two months behind the temperature minimum, reflecting a balance between thermally driven oxygen solubility increases and biologically driven oxygen production. Minimum [O_2] in that near-surface interval (October in the Northern Hemisphere and March/April in the Southern Hemisphere) is more coincident with the temperature maximum, reflecting primary control by thermally driven oxygen solubility decreases. The amplitude of the [O_2] seasonal cycle is about 2.3 μmol kg^{-1} in an intermediate interval (100–600 dbars) and about 0.2 μmol kg^{-1} in a deep interval (600–2000 dbars).

https://doi.org/10.5194/essd-2022-308
Preprint. Discussion started: 20 September 2022

The timing of maximum [O_2] values is similar between the near-surface interval and intermediate interval in both hemispheres, indicating the well-mixed nature of the ocean in winter and early spring when [O_2] is high. On the other hand, minimum [O_2] in the intermediate interval lags behind that in the near-surface interval in both hemispheres, possibly reflecting higher stratification in the upper ocean when temperatures are warmer and/or the remineralization of sinking organic matter after summer production. Further analysis of climatological [O_2] cycles from GOBAI-O_2 can provide insight into the physical and biological factors that control surface and subsurface oxygen on regional and global scales.

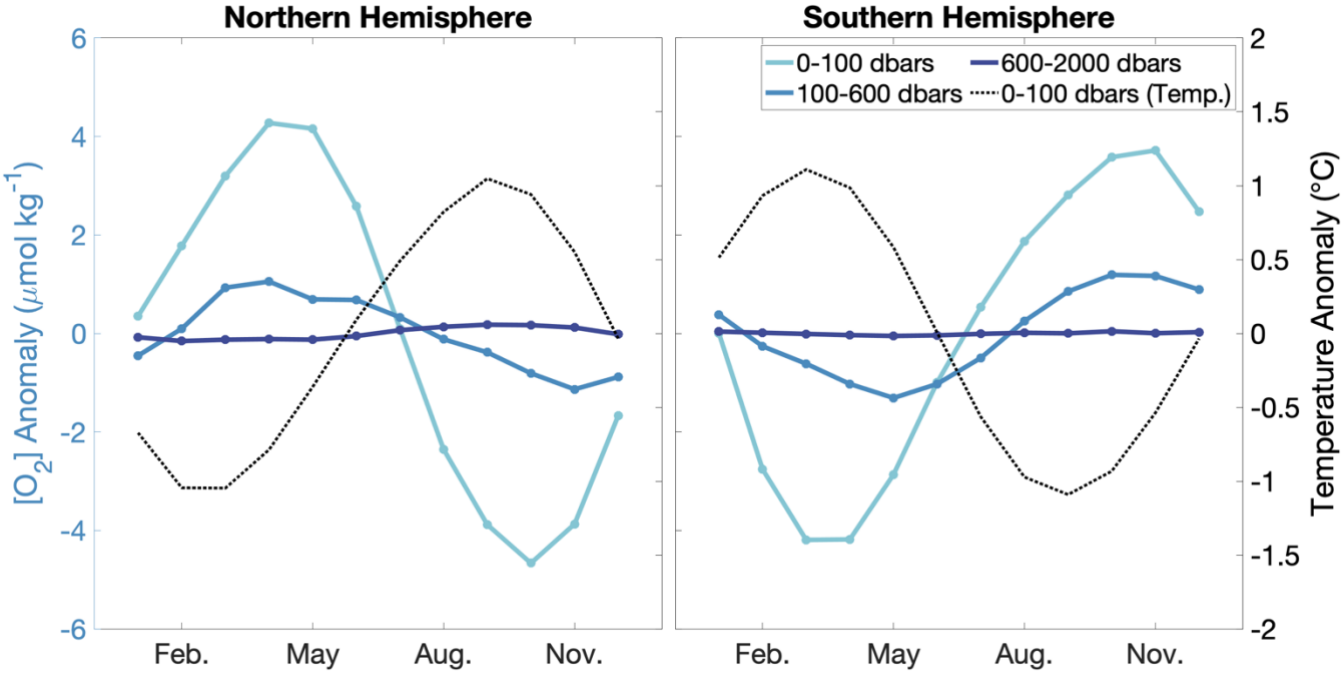

Figure 6. Climatological cycles of [O_2] anomalies (monthly [O_2] minus long-term mean [O_2]) integrated globally over three pressure intervals: 0–100, 100–500, and 500–2000 dbars. The dotted line shows climatological temperature anomaly integrated globally over the 0–100 dbar interval.

3.2.3 Interannual oxygen variability

Deoxygenation is evident in GOBAI-O_2 over the past two decades, coincident with ocean warming (Fig. 7). The spatially weighted rate of deoxygenation in the upper two kilometers globally (along with a 90% confidence interval) is −1.15 ± 0.26 μmol kg^{-1} dec.$^{-1}$ (−0.77 ± 0.17 % dec.$^{-1}$). The rate of deoxygenation in GOBAI-O_2 varies over depth, with a near-surface interval (0–100 dbars) displaying a trend in [O_2] of −1.00 ± 0.58 μmol kg^{-1} dec.$^{-1}$ (−0.45 ± 0.26 % dec.$^{-1}$), an intermediate interval (100–600 dbars) −0.82 ± 0.59 μmol kg^{-1} dec.$^{-1}$ (−0.51 ± 0.37 % dec.$^{-1}$), and a deep interval (600–2000 dbars) −1.27 ± 0.50 μmol kg^{-1} dec.$^{-1}$ (−0.90 ± 0.29 % dec.$^{-1}$). Interannual variability is greatest in the near-surface interval: when the multi-

https://doi.org/10.5194/essd-2022-308
Preprint. Discussion started: 20 September 2022

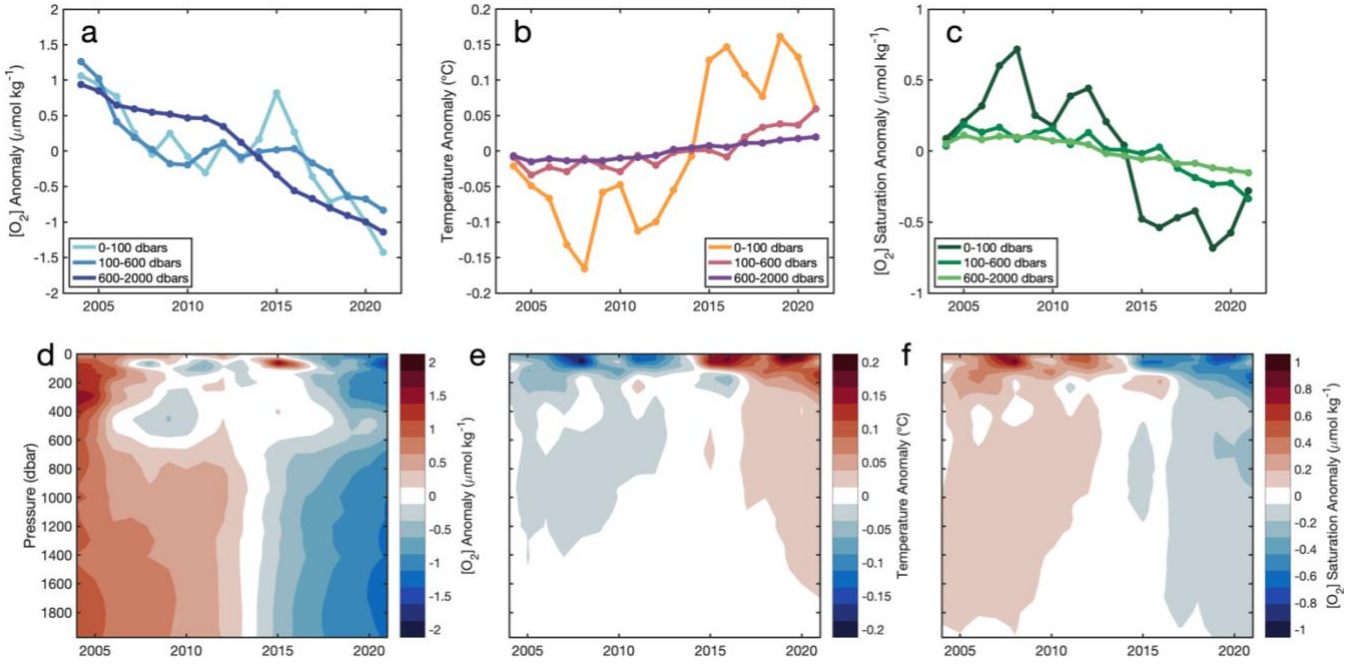

Figure 7. Annual mean (a) [O_2] anomalies from GOBAI-O_2, (b) temperature anomalies from RG09, and (c) [O_2]$_{sat.}$ anomalies calculated from RG09 (anomalies calculated as annual means minus the long-term mean) integrated globally over three pressure intervals: 0–100, 100–600, and 600–2000 dbars. Hovmöller diagrams showing annual mean (d) [O_2] anomalies from GOBAI-O_2, (e) temperature anomalies from RG09, and (f) [O_2]$_{sat.}$ anomalies calculated from RG09 over depth from 2004 to 2021.

Ocean warming has a direct effect on oxygen concentrations by lowering the solubility of O_2 in ocean water (Garcia and Gordon, 1992). Solubility changes explain about 65% of deoxygenation in the near-surface ocean interval (0–100 dbars), 32% in the intermediate ocean interval (100–600 dbars), and 13% in the deep ocean interval (600–2000 dbars) (Fig. 7c and 7f). The remaining deoxygenation must then be caused by indirect consequences of ocean warming (such as increased ocean stratification) or other processes, including changes to oxygen utilization and ocean ventilation variability (Oschlies et al., 2018), the magnitudes of which this analysis does not attempt to deconvolve. It's important to note that the RG09 temperature and salinity fields are constructed such that they relax toward the climatological means during periods of low data density. For this reason, temperature is biased somewhat high (Figs. 7b and 7e) and therefore O2 solubility biased somewhat low (Figs. 7c

https://doi.org/10.5194/essd-2022-308
Preprint. Discussion started: 20 September 2022

and 7f) toward the beginning of the time series when fewer observations are available. This artifact is not reflected in GOBAI-O_2 (Figs. 7a and 7d); whereas GOBAI-O_2 was constructed using the RG09 temperature and salinity fields, temporal information included in the training and application of the ML algorithms allows for the trend inherent to the underlying oxygen data to be retained.

GOBAI-O_2 trends can be viewed in the context of other recent analyses that explore long term changes in ocean oxygen. From the surface to 1000 dbars, the GOBAI-O_2 trend of −0.60 ± 0.25 % dec.$^{-1}$ from 2004–2021 is comparable to that assessed by Bindoff et al. (2019) of −0.48 ± 0.35 % dec.$^{-1}$ from 1970–2010 (surface to 1000 meters), which takes into account estimates from Helm et al. (2011) (−0.44 ± 0.14 % dec.$^{-1}$), Schmidtko et al. (2017) (−0.34 ± 0.35 % dec.$^{-1}$), and Ito et al. (2017) (−0.68 ± 0.33 % dec.$^{-1}$). In the surface interval, the GOBAI-O_2 trend of −0.45 ± 0.26 % dec.$^{-1}$ is larger than, though within uncertainties of, the Bindoff et al. (2019) assessment of −0.28 ± 0.24 % dec.$^{-1}$; in the intermediate interval the GOBAI-O_2 trend of −0.51 ± 0.37 % dec.$^{-1}$ is comparable to the Bindoff et al. (2019) assessment of −0.52 ± 0.36 % dec.$^{-1}$. While these comparisons represent different periods of time such that one should not expect perfect agreement, we find the consistency encouraging. The comparison not only places the GOBAI-O_2 trends in a longer term context but suggests that the enhanced observations and analysis result in a reduced trend uncertainty despite the comparatively-shorter 18-year record (± 0.25 % dec.$^{-1}$) versus the longer but more sparse 40-year record available to Bindoff et al. (± 0.35 % dec.$^{-1}$; 2019).

Finally, the trends presented here represent both natural and potentially anthropogenic variability over the interval between 2004 and 2021, and should not be interpreted to be driven exclusively by ocean warming and other associated impacts of anthropogenic climate change. This is especially true of the regional trends. The period of time examined is relatively short and the domain is not inclusive of the entire global ocean. Accordingly, decadal-scale variability in ocean ventilation, interior circulation, and biological oxygen utilization may exert significant influence over these trends.

3.2.4 Uncertainty

GOBAI-O_2 uncertainty fields, which were estimated as described in section 2.5, can be used to assess confidence in multi-year trends and seasonal cycles of [O_2], both on a global and regional scale. Time-averaged uncertainty fields at 150 dbar (Fig. 8) suggest that the largest contributor overall is the algorithm uncertainty, though it is also the most geographically variable. Averaged globally over space and time, $u([O_2])_{meas.}$ was equal to 2.3 μmol kg^{-1} (2.8 μmol kg^{-1} on the 150 dbar level), $u([O_2])_{grid.}$ was equal to 2.4 μmol kg^{-1} (4.8 μmol kg^{-1} on the 150 dbar level), and $u([O_2])_{alg.}$ was equal to 3.9 μmol kg^{-1} (6.7 μmol kg^{-1} on the 150 dbar level). Combined, $u([O_2])_{tot.}$ (Eq. 1) was equal to 5.9 μmol kg^{-1} (9.7 μmol kg^{-1} on the 150 dbar level), which is comparable to the global average RMSD of 6.2 μmol kg^{-1} determined independently by withholding data from algorithm training (Table 2, Fig 2a-2c).

https://doi.org/10.5194/essd-2022-308
Preprint. Discussion started: 20 September 2022

Measurement uncertainty provides an estimate of confidence in an [O_2] value assigned to a water sample by direct measurement; gridding uncertainty provides an estimate of confidence that the [O_2] value provided for a four-dimensional grid cell might represent [O_2] at any point in time and space within that grid cell; and algorithm uncertainty provides an estimate of confidence that the predicted [O_2] value for a given grid cell is appropriate as the average value for that grid cell. Algorithm uncertainty in particular depends upon the distribution of data available to train the ML algorithms and the ability of the trained algorithms to represent underlying variability in the system. Here, algorithm uncertainty was assessed via the exercise with synthetic data from GFDL-ESM4 (see sections 2.3 and 3.1.2).

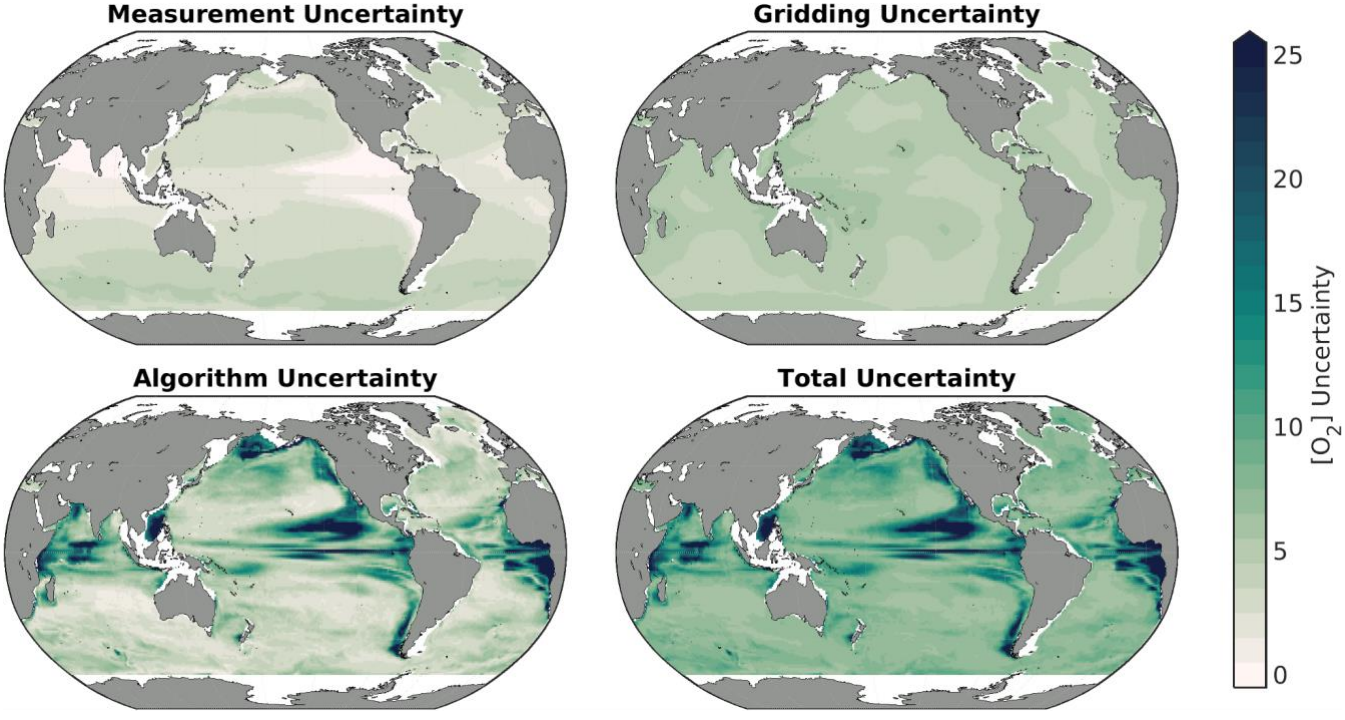

Figure 8. Long-term means of the uncertainty contributors to GOBAI-O_2 on the 150 dbar pressure level.

Algorithm uncertainty should in general decrease as the spatiotemporal coverage of available training data increases. Regionally, the uncertainty depends upon the degree to which the underlying variability of the system is captured by the available training observations and the ability of the ML algorithms to reconstruct that variability from concurrent measurements of other seawater properties. The fact that algorithm uncertainty is the largest uncertainty contributor in GOBAI-O_2 suggests that limitations in the ML algorithms used to fill spatiotemporal gaps in [O_2] outweigh limitations related to measurement quality and averaging data to four-dimensional bins. Comparing the Δ[O_2] map in Fig. 2f or the algorithm uncertainty map in Fig. 8 to the data distribution map in Fig. 1 or Fig. A1 suggests that sparse sampling is primarily to blame for these limitations: clusters of high uncertainties tend to occur where observations are limited. Detailed analysis of GFDL-

https://doi.org/10.5194/essd-2022-308
Preprint. Discussion started: 20 September 2022

ESM4 water mass characteristics in the California Current System has also revealed that high uncertainties occur where water masses with similar physical characteristics but different oxygen signatures mix, underscoring that the measurement of additional biogeochemical parameters can supplement the physical/spatiotemporal-based [O_2] estimates presented here. Overall, the dominance of algorithm uncertainty is consistent with uncertainty analysis conducted for gap-filling methods applied to other ocean biogeochemical variables (e.g., Landschützer et al., 2014; Gregor and Gruber, 2020). For this reason, continued expansion of oxygen observations in undersampled regions will be critical to reduce uncertainty in our gap filling, and ultimately our understanding, of the global subsurface oxygen evolution.

Global mean depth profiles of uncertainty contributors (Fig. A10) emphasize the general attenuation of uncertainty away from the surface, with subsurface maxima of algorithm uncertainty at 200 dbars and total uncertainty at 130 dbars. These maxima correspond to depths at which vertical gradients in [O_2] are relatively high (see Fig. 4). Here, small variations in the depths of density surfaces can influence [O_2] on a given depth level; this variability is challenging to capture, even with potential density as a predictor variable in the ML models (see Table 1).

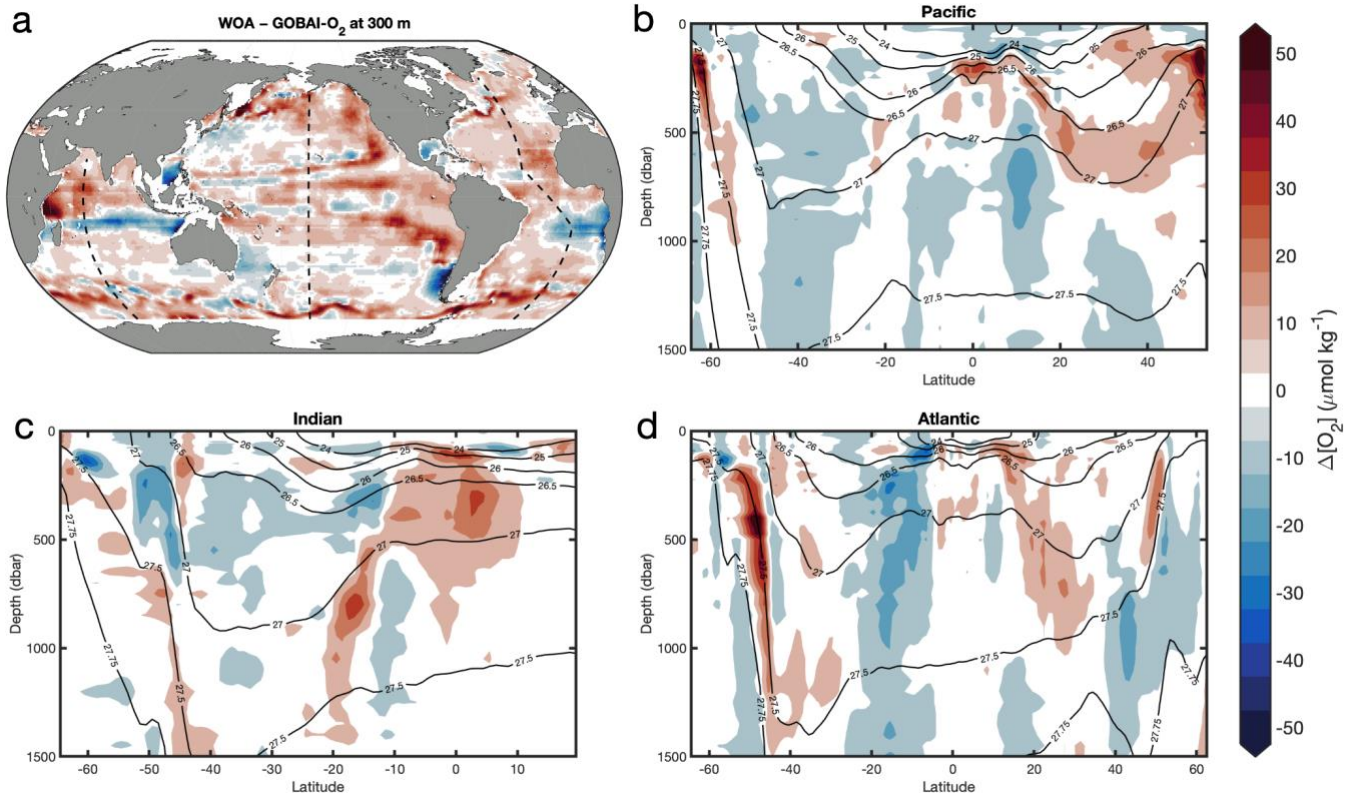

Figure 9. The difference between climatological mean [O_2] from WOA18 and long-term mean [O_2] from GOBAI-O_2 ($\Delta[O_2] = [O_2]_{WOA} - [O_2]_{GOBAI}$) at 300 meters (a) and from the surface to 1500 dbars in the Pacific (b), Indian (c), and Atlantic (d) Oceans.

https://doi.org/10.5194/essd-2022-308
Preprint. Discussion started: 20 September 2022

3.2.5 Comparison to World Ocean Atlas

Long-term mean fields of [O_2] from GOBAI-O_2 were compared to corresponding climatological mean fields from WOA18 (Fig. 9). On average, GOBAI-O_2 oxygen concentration is nearly 10 µmol kg^{-1} lower than WOA18. This can be partly explained by the fact that GOBAI-O_2 is centered on the year 2012 whereas WOA18 takes into account [O_2] observations dating back to 1955, and global deoxygenation has occurred in recent decades (Bindoff et al., 2019). Additionally, the World Ocean Atlas has been demonstrated to overestimate [O_2] in suboxic zones (Bianchi et al., 2012), potentially contributing to the discrepancy as well. Spatially, the largest differences do indeed occur within and especially near the boundaries of oxygen minimum zones, as well as along $\sigma = 27.5$ kg m^{-3} in the Southern Ocean.

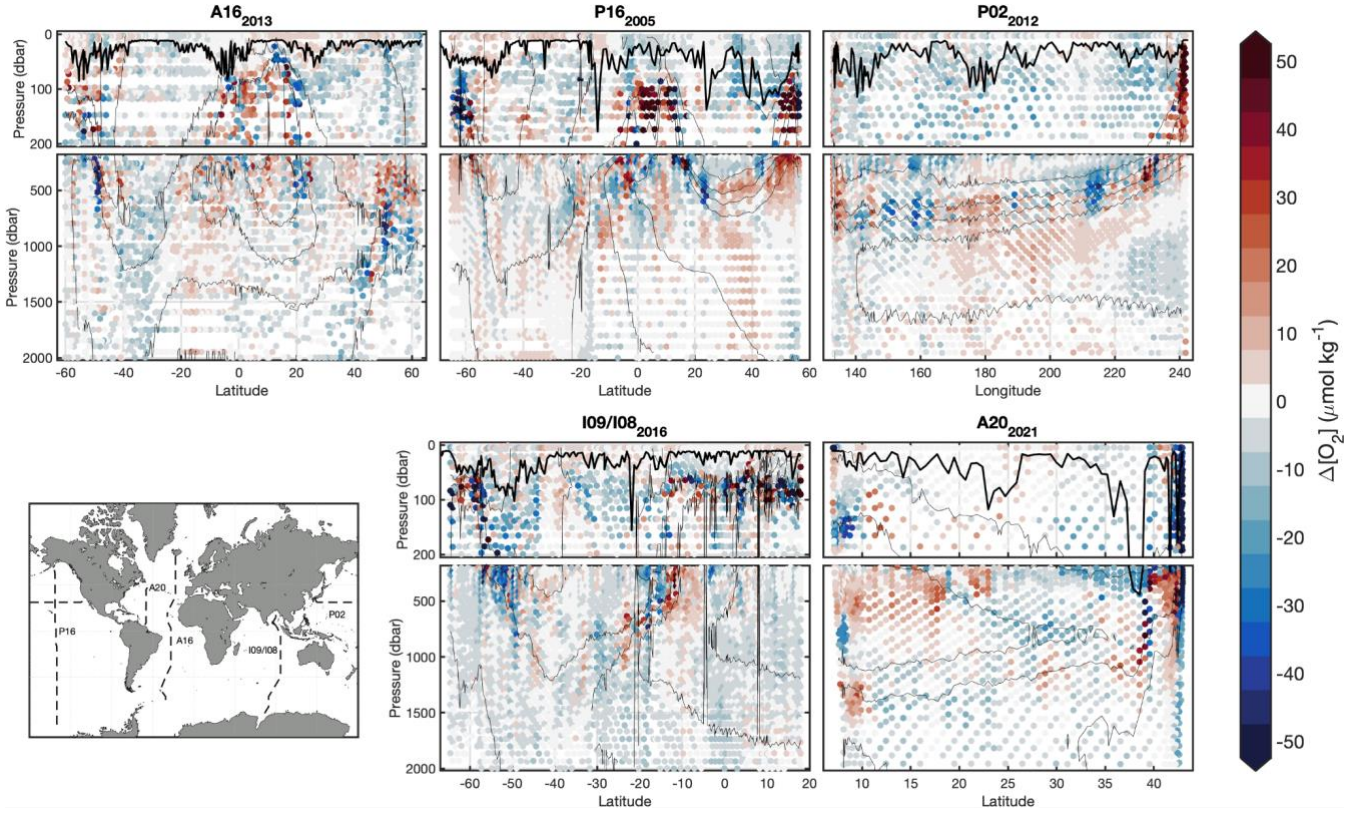

Figure 10. Section plots displaying comparisons between discrete observations of [O_2] from repeat hydrography cruises and [O_2] extracted from corresponding grid cells in GOBAI-O_2. Thick lines in each panel represent mixed layer depth calculated as the depth at which potential density anomaly increased to 0.03 kg m^{-3} greater than potential density anomaly at 10 dbars. Thin lines are contours representing increments of 50 µmol kg^{-1} in [O_2].

https://doi.org/10.5194/essd-2022-308
Preprint. Discussion started: 20 September 2022

3.2.6 Comparison to independent measurements

GOBAI-O_2 was compared to direct observations from repeat hydrography cruises, including meridional transects across the Atlantic (A16 in 2013 and A20 in 2021), Pacific (P16 in 2005), and Indian (I08 and I09 in 2016) Oceans, as well as a zonal transect across the Pacific Ocean (P02 in 2012). This exercise assessed how well monthly [O_2] estimates from GOBAI-O_2 were able to represent high-quality [O_2] measurements at distinct points in time. Observations from all but one of these cruises (A20 in 2021) were used in the development of GOBAI-O_2.

For the cruise datasets examined, GOBAI-O_2 estimates matched fairly well with discrete measurements in the mixed layer and below ~1000 dbars (Fig. 10). In intermediate depths, however, large differences occasionally occur. These large differences tended to cluster around areas with strong vertical gradients in [O_2] (thin contours in Fig. 10 represent increments of 50 µmol in [O_2]). Comparison of Fig. 10 to Fig. A11 gives confidence to our uncertainty evaluation: larger differences between discrete measurements and GOBAI-O_2 occur where $u([O_2])^2_{tot.}$ is large. Median biases, mean biases, and RMSDs between direct observations and GOBAI-O_2 are given in Table B5.

4 Conclusions

GOBAI-O_2 is a major step toward the fulfilment of the primary goal set out by Gruber et al. (2010): "to determine, on a global-scale, seasonal to decadal time-scale variations in dissolved oxygen concentrations throughout the upper ocean". Quantifying these variations is important for documenting ocean deoxygenation, determining global net primary productivity and carbon export, and facilitating studies of the oceanic uptake of anthropogenic CO_2. In addition, insights into ocean biogeochemical dynamics when observations are unavailable often come from ocean models, and GOBAI-O_2 can bring value to modelling studies by providing fields of [O_2] to be used for boundaries and initialization. This all being said, the uncertainty analysis conducted here confirms that GOBAI-O_2 remains limited, primarily by sparse sampling. The most consequential action to improve GOBAI-O_2 fields over the next decade will be the continued deployment of Argo floats with oxygen optodes — emphasizing the importance of bolstering the biogeochemical Argo array and expanding the international OneArgo network into high latitudes, the deep ocean, and marginal seas (Roemmich et al., 2019; 2021; Schofield et al., 2022) — and the continued collection of discrete dissolved oxygen observations, primarily through the international GO-SHIP program.

Besides the collection of more observations, additional actions can be taken to improve GOBAI-O_2 fields. For one, more predictor variables and ML algorithms can be tested. Different processes dominate [O_2] variability in different regions (Keeling et al., 2010; Oschlies et al., 2018; Garcia-Soto et al., 2021), and certain predictor variables will be better suited for capturing these processes. Also, ML algorithms adapt to data sparseness and modes of variability in different ways (Ritter et al., 2017; Gregor et al., 2019), so estimates in a given region that are worse using one algorithm may be better using another. Therefore,

https://doi.org/10.5194/essd-2022-308
Preprint. Discussion started: 20 September 2022

555 regionally-tuned predictors and more diverse ensembles of ML algorithms should lead to increased confidence in estimates of ocean interior [O_2].

Another action that could result in improved fidelity of GOBAI-O_2 fields is the use of predictor variable fields with higher resolution across sharp biogeochemical gradients, especially with respect to depth. Ocean profiles of temperature and salinity
560 tend to be relatively smooth, so a depth resolution on the order of tens of meters in the upper ocean increasing to hundreds of meters at depth is sufficient for gridded products. Biogeochemical parameters like oxygen, on the other hand, tend to be characterized by profiles with sharp gradients and with distinct minima and maxima in the water column (Sarmiento and Gruber, 2006). These minima and maxima can occur very near the surface or hundreds of meters below it. For this reason, comparisons of GOBAI-O_2 to direct measurements of [O_2] can be uniquely problematic in the ~100–1000 dbar range when
565 sharp gradients are present (Fig. 10). Overcoming this issue could involve the development of temperature and salinity fields with higher resolution across depth ranges with sharp biogeochemical gradients. Alternatively, [O_2] estimates could be made using temperature and salinity observations at their original resolution, then mapped onto four-dimensional grids that are uniquely suited in their spatial resolution for biogeochemical parameters. A necessary consideration of the latter option would be computing resources: applying complex ML algorithms to temperature and salinity measurements from Argo floats at their
570 original resolution may prove to be impractical.

Finally, observations from additional platforms could be incorporated into schemes like this one to map [O_2] in the global ocean. Ocean gliders and moored profilers have long been equipped with oxygen optodes. These platforms collect data at unique spatiotemporal scales and could add predictive information for [O_2] that is not provided by Argo float observations or
575 discrete shipboard measurements. To facilitate the incorporation of new data streams into the development of gridded data products, accessible databases should be created and maintained (Testor et al., 2019; Grégoire et al., 2022).

The method used to develop GOBAI-O_2 can be applied in a similar way to other ocean chemical parameters. In addition to dissolved oxygen, the BGC Argo program has deployed floats with sensors for measuring dissolved nitrate, pH, chlorophyll-
580 a, particle backscatter, and downwelling irradiance. Machine learning methods have been used to develop four-dimensional fields of optical properties, i.e. chlorophyll-a and particle backscatter (Sauzède et al., 2015; 2016), and continued refinement of those fields is ongoing (Sauzède et al., 2021). Chemical properties, i.e. nitrate and pH, that exhibit distributions more similar to [O_2] are good candidates for adoption into the GOBAI mapping scheme. Together with property estimation algorithms for TA (Bittig et al., 2018b; Carter et al., 2021), a mapped ocean interior pH product could be used to resolve the entire ocean
585 carbonate system in four dimensions in near real time.

Ultimately, global changes to the amount of dissolved oxygen in ocean waters will have profound effects on the metabolism of marine organisms (Pörtner and Farrell, 2008; Sampaio et al., 2021) and the cycling of biogeochemically important elements

https://doi.org/10.5194/essd-2022-308
Preprint. Discussion started: 20 September 2022


Open Access Earth System Science Data Discussions

(Gruber, 2004; Berman-Frank et al., 2008). Whereas ocean models agree that the ocean's oxygen inventory has been declining and will continue to decline, disagreement remains as to regional patterns of this deoxygenation. Direct observations are critical for the confirmation or contradiction of model trends. With this work we have turned to autonomous and discrete observations, with the assistance of machine learning algorithms, to produce and analyze a multi-year gridded product of ocean dissolved oxygen called GOBAI-O_2. We independently confirm a phenomenon that has been demonstrated previously — the ocean is losing dissolved oxygen at a rapid rate — and provide an observation-based product that can be compared to new and existing observational and model-based reconstructions of ocean deoxygenation.

https://doi.org/10.5194/essd-2022-308
Preprint. Discussion started: 20 September 2022

Open Access Earth System Science Data Discussions

5 Appendices

Appendix A. Supplemental Figures

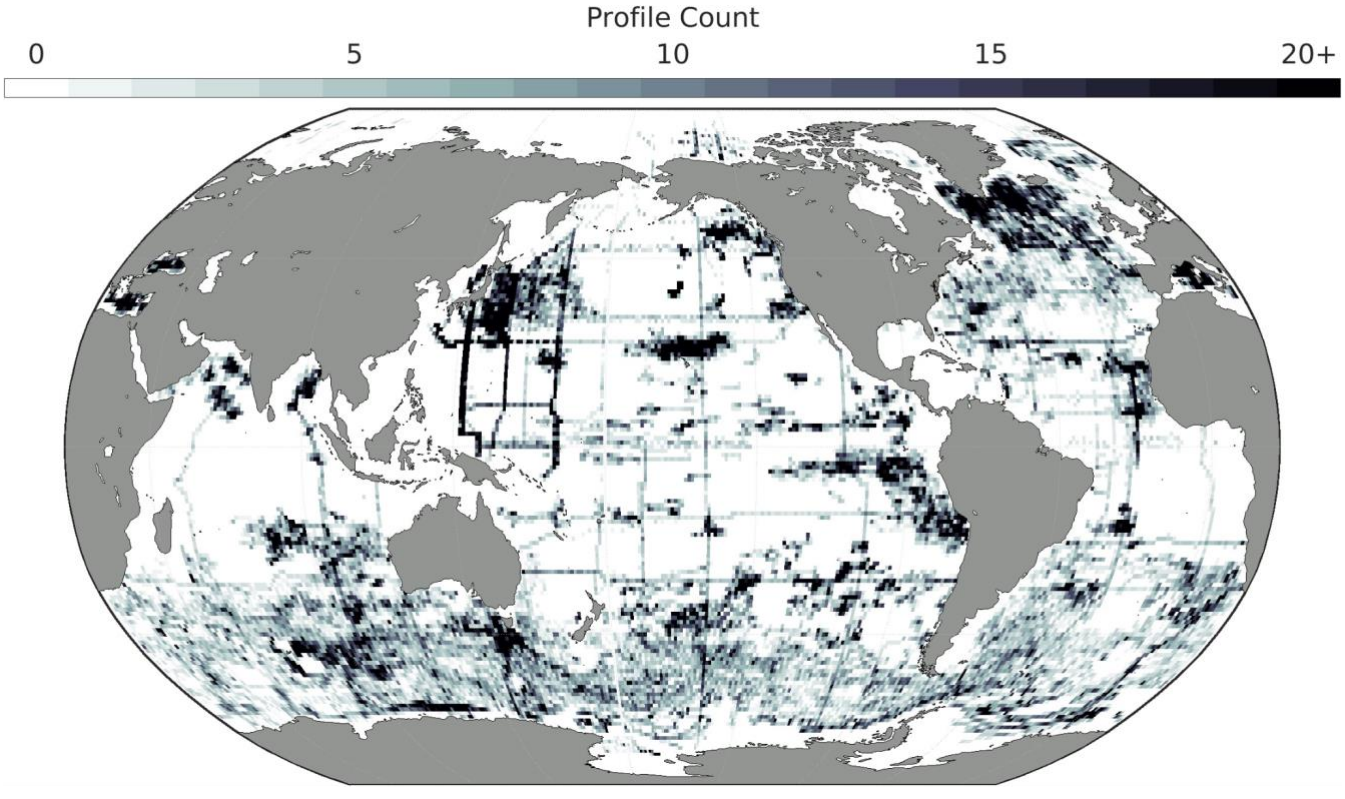

Figure A1. The number of profiles (either ship-based or Argo float-based) contained within each 1° x 1° box in the global ocean.

https://doi.org/10.5194/essd-2022-308
Preprint. Discussion started: 20 September 2022

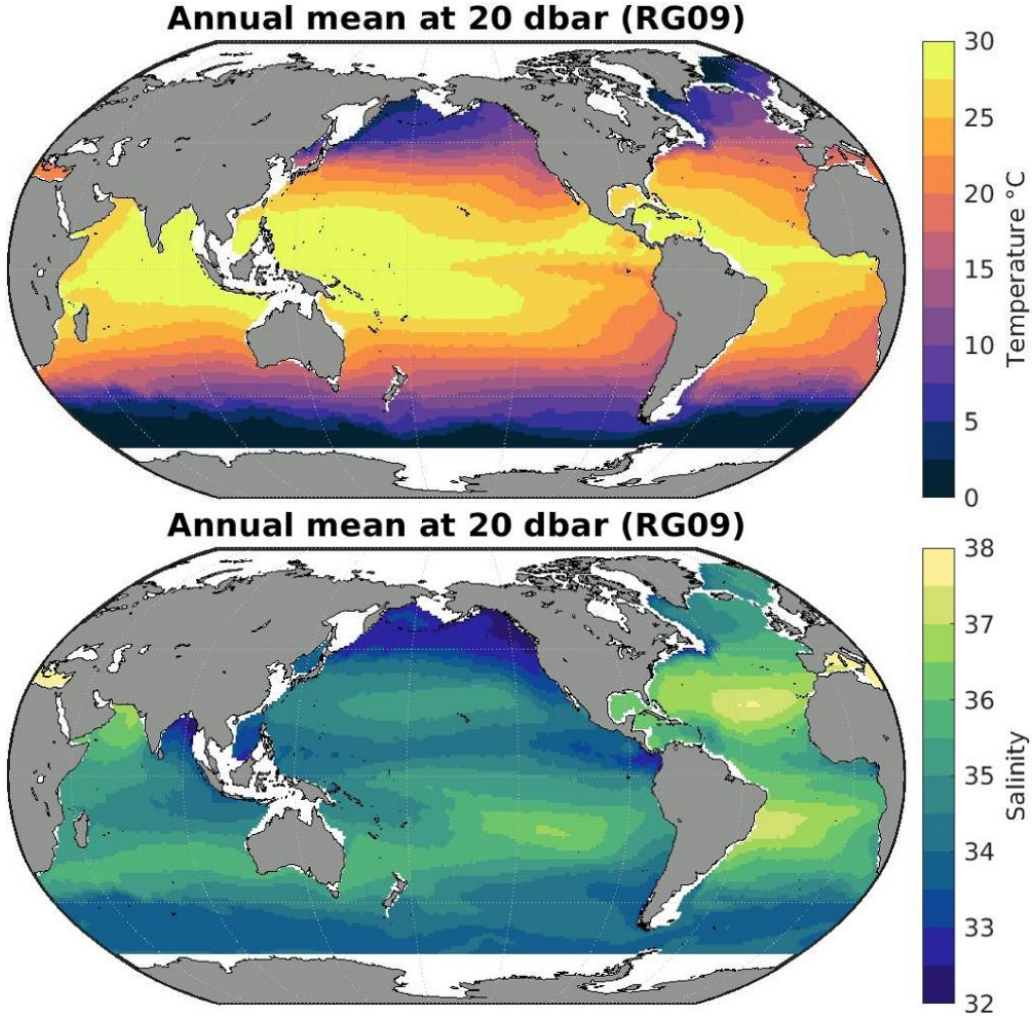

Figure A2. Annual mean in situ temperature (top) and salinity (bottom) from RG09 (2004–2021) at 20 dbars.

https://doi.org/10.5194/essd-2022-308
Preprint. Discussion started: 20 September 2022

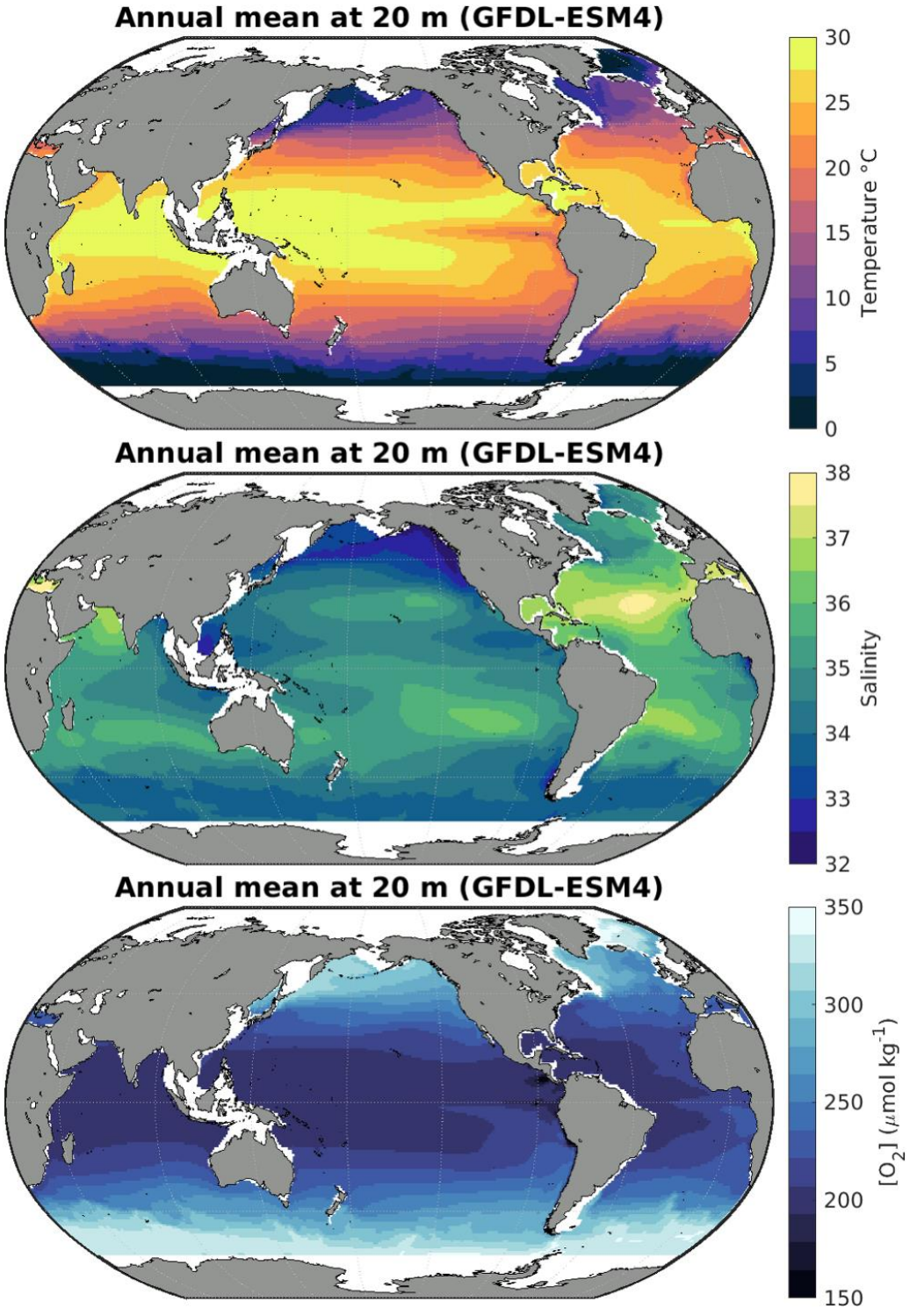

Figure A3. Annual mean in situ temperature (top), salinity (middle), and dissolved oxygen concentration (bottom) from GFDL-ESM4 (2004–2021) at 20 meters.

https://doi.org/10.5194/essd-2022-308
Preprint. Discussion started: 20 September 2022

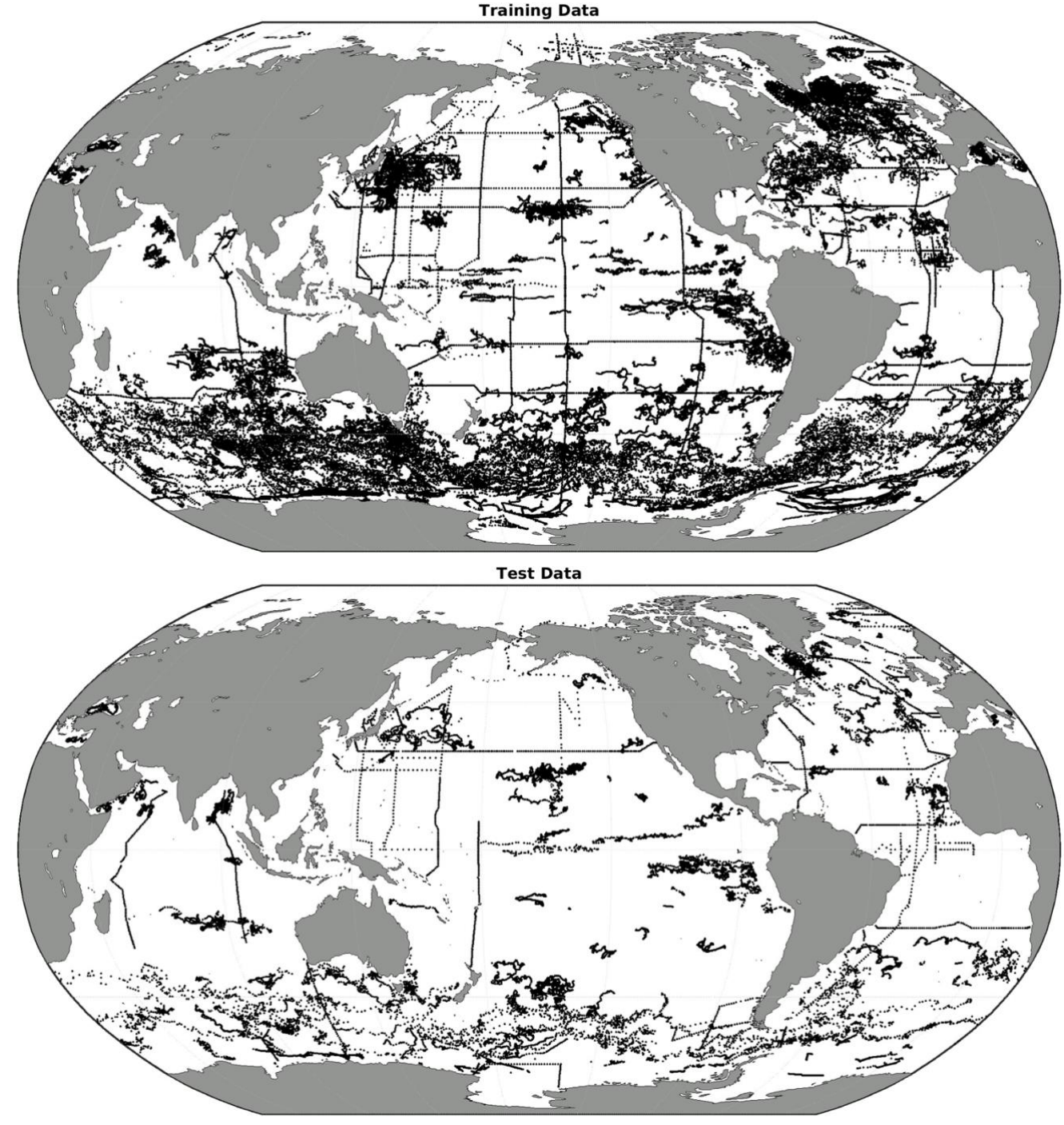

Figure A4. The spatial distribution of profile data used to train (a) and test (b) $RFR_{Data\text{-}Eval}$ and $FNN_{Data\text{-}Eval}$ algorithms.

https://doi.org/10.5194/essd-2022-308
Preprint. Discussion started: 20 September 2022

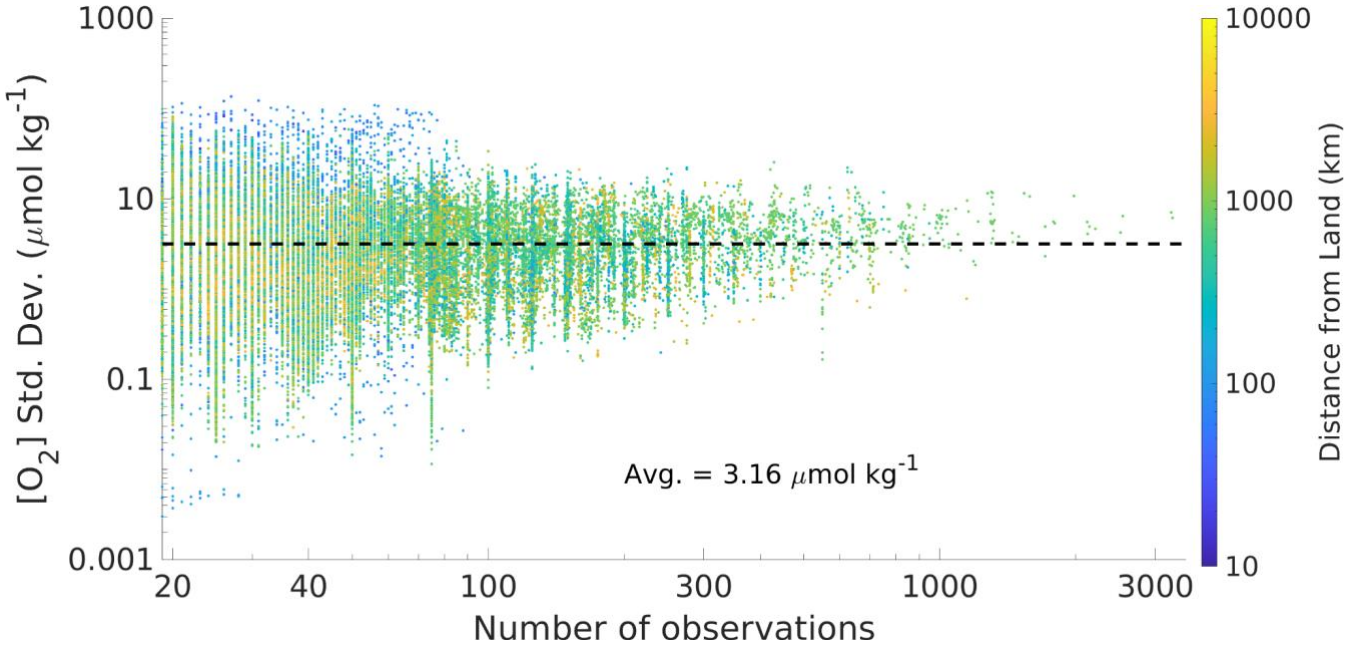

Figure A5. A comparison between the number of observations binned within a four-dimensional grid cell and the standard deviation in [O_2] among those observations. The horizontal black line shows the mean standard deviation (3.16 µmol kg^{-1}). The points are colored by distance from land, with the cluster of high-variability blue data emphasizing that the grid cells with particularly high standard deviations are coastally biased.

https://doi.org/10.5194/essd-2022-308
Preprint. Discussion started: 20 September 2022

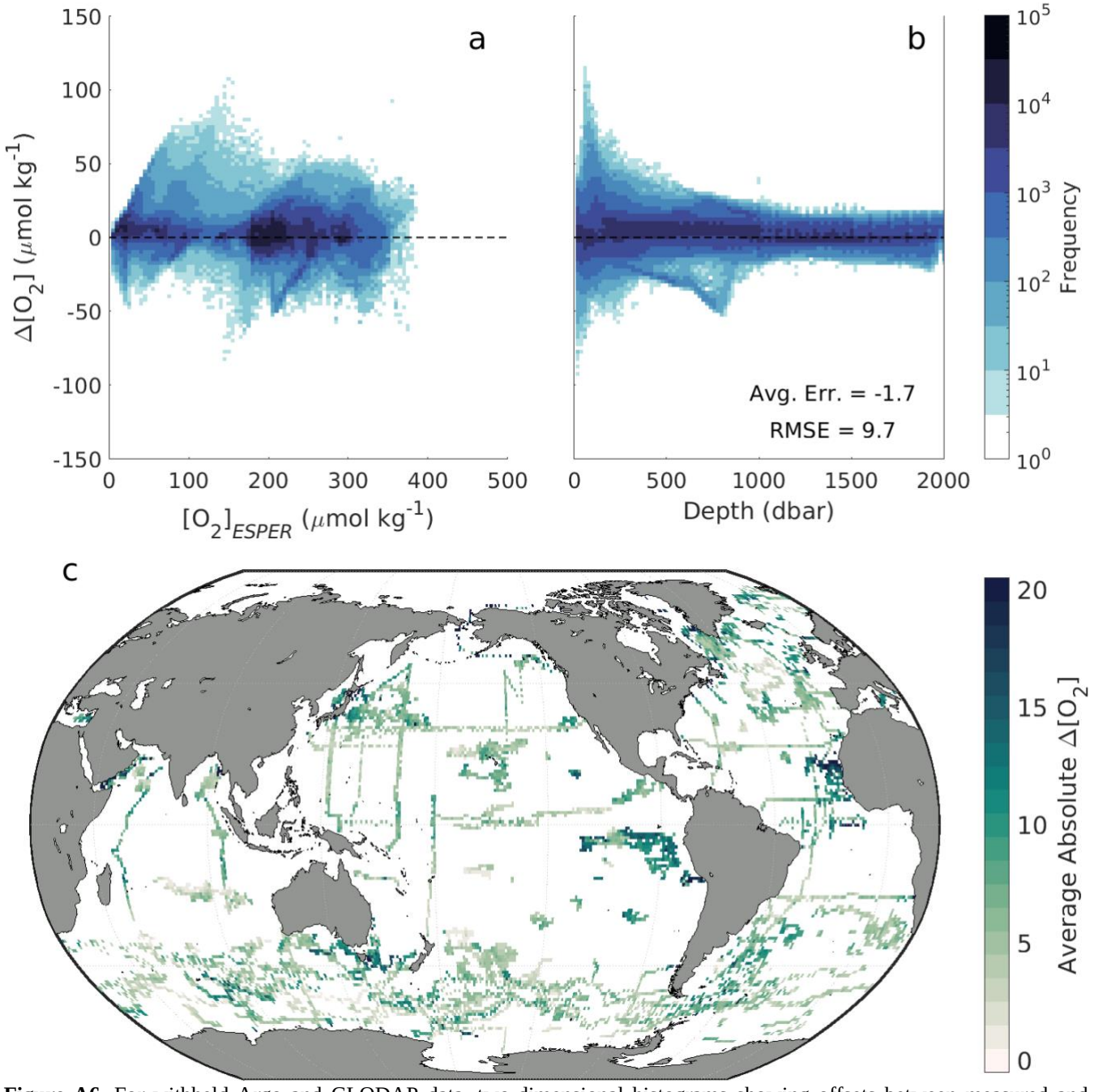

Figure A6. For withheld Argo and GLODAP data, two-dimensional histograms showing offsets between measured and ESPER-Mixed-calculated oxygen ($\Delta[O_2] = [O_2]_{meas} - [O_2]_{ESPER}$) as a function of (a) $[O_2]_{ESPER}$ and (b) pressure in the water column. (c) Absolute $\Delta[O_2]$ values averaged over depth and time for 1° latitude by 1° longitude grid cells in the global ocean.

https://doi.org/10.5194/essd-2022-308
Preprint. Discussion started: 20 September 2022

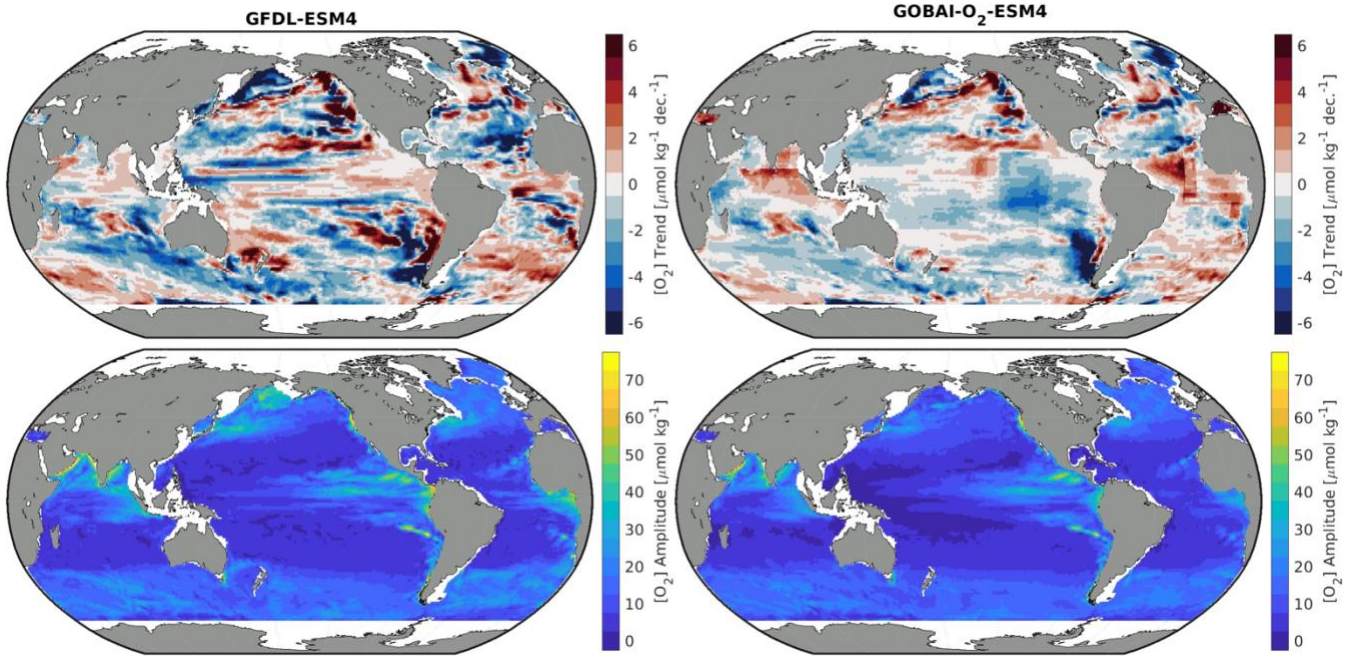

Figure A7. Trends in annual mean [O_2] integrated from 200 to 1000 dbars (top figures) and climatological amplitude in monthly mean [O_2] integrated from 0 to 200 dbars (bottom figures) for GFDL-ESM4 (left figures) and GOBAI-O_2-ESM4 (right figures).

https://doi.org/10.5194/essd-2022-308
Preprint. Discussion started: 20 September 2022

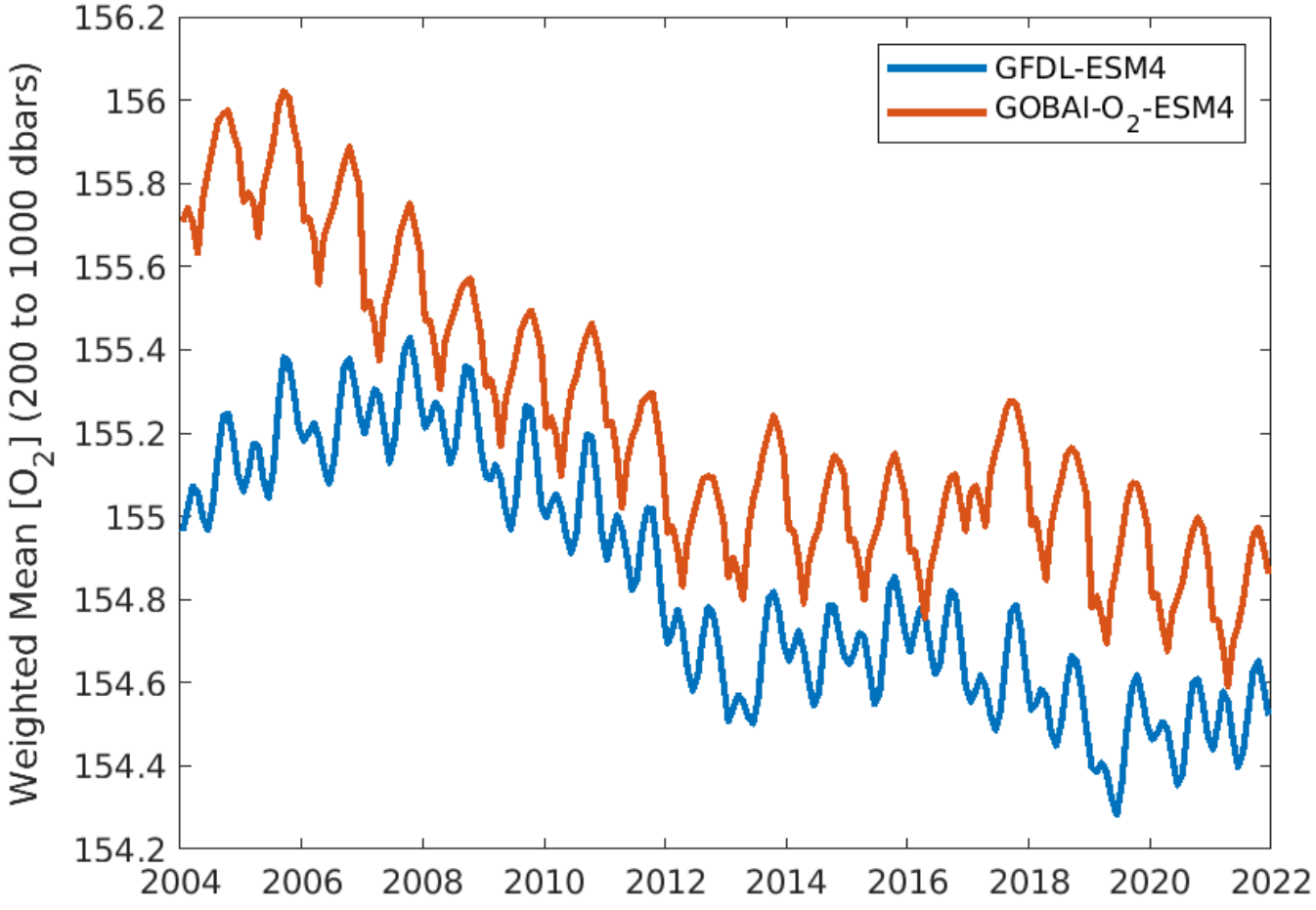

Figure A8. Monthly area-weighted mean [O_2] integrated globally from 200 to 1000 dbars from GFDL-ESM4 (blue) and GOBAI-O_2-ESM4 (orange).

https://doi.org/10.5194/essd-2022-308
Preprint. Discussion started: 20 September 2022

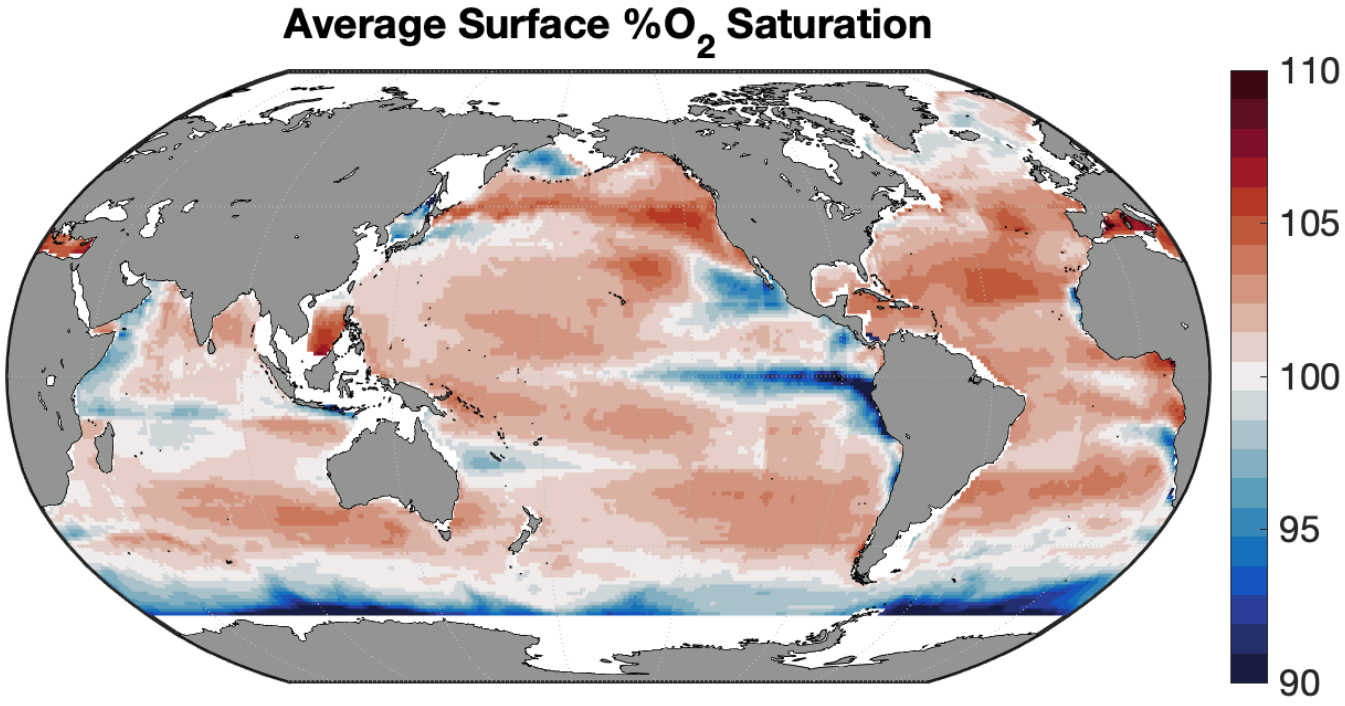

Figure A9. Long-term mean percent oxygen saturation on the uppermost pressure level in GOBAI-O_2.

https://doi.org/10.5194/essd-2022-308
Preprint. Discussion started: 20 September 2022

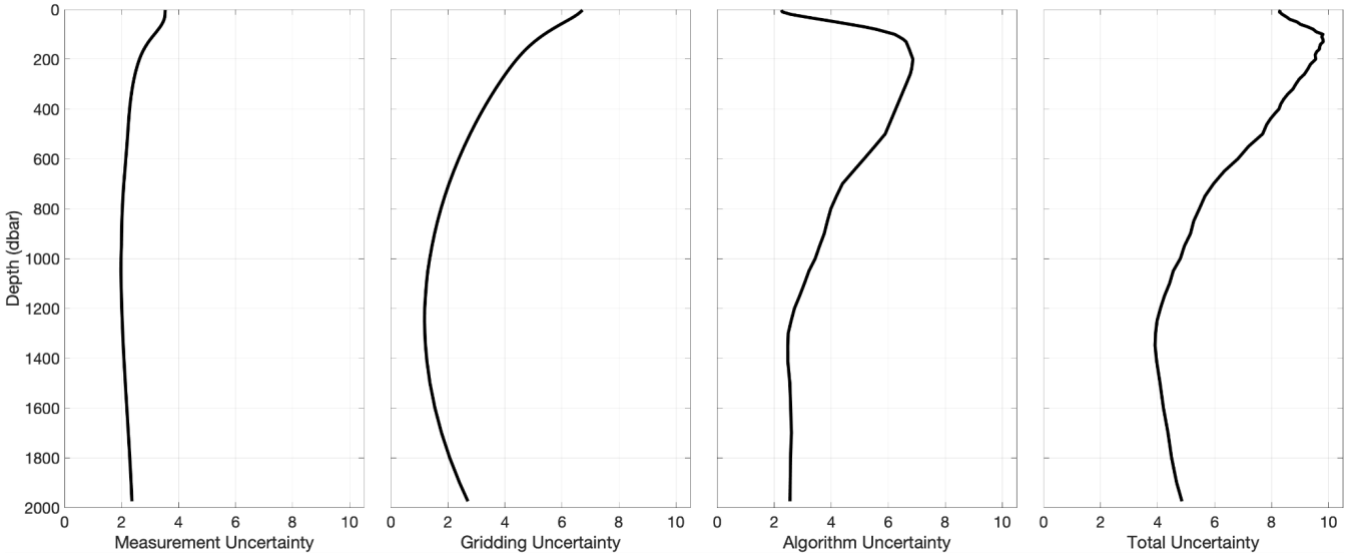

Figure A10. Global mean depth profiles of uncertainty contributors to GOBAI-O_2.

https://doi.org/10.5194/essd-2022-308
Preprint. Discussion started: 20 September 2022

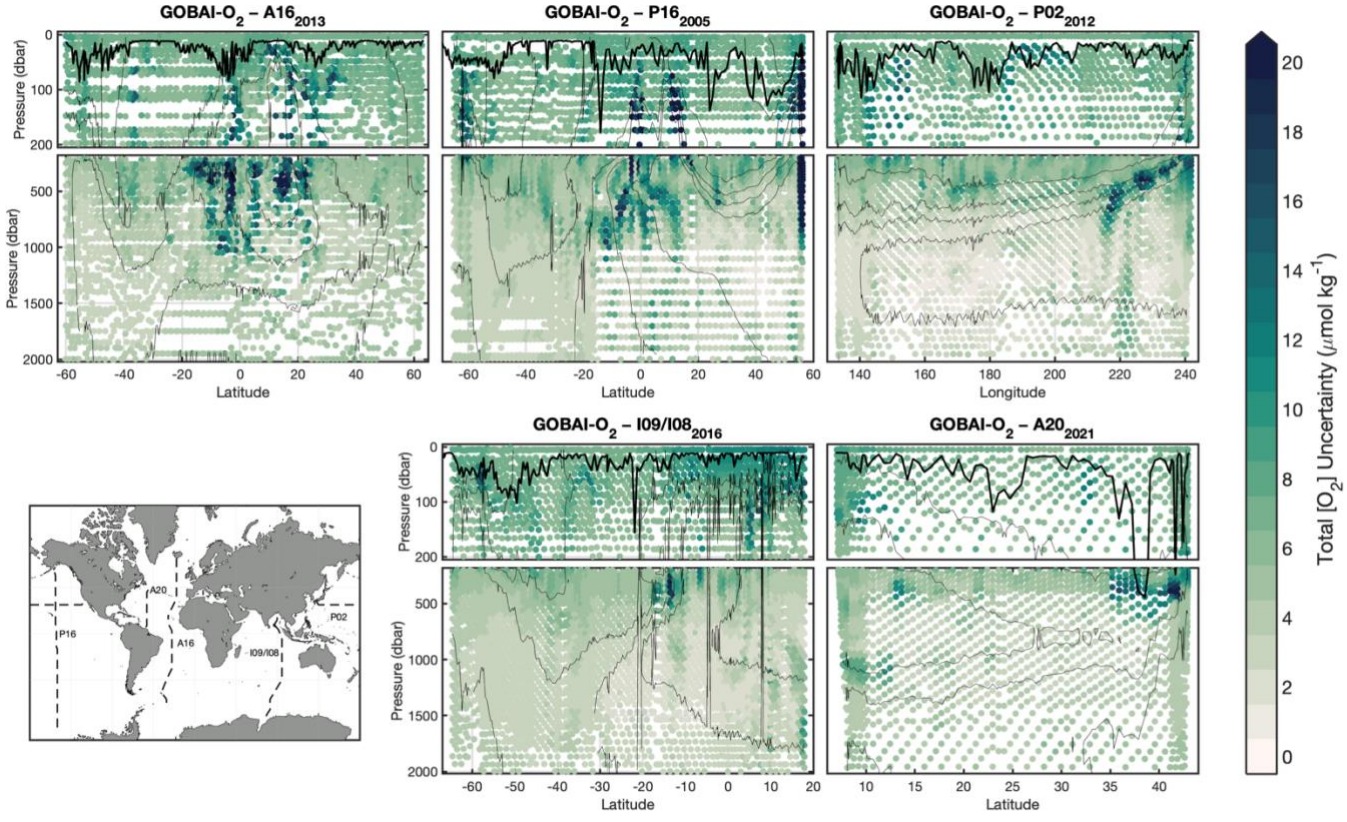

Figure A11. Section plots displaying total uncertainty estimates from GOBAI-O_2 that correspond to discrete measurements of [O_2] from repeat hydrography cruises.

https://doi.org/10.5194/essd-2022-308
Preprint. Discussion started: 20 September 2022

Open Access Earth System Science Data Discussions

Appendix B. Supplemental Tables

Table B1. Boundaries for the seven large ocean regions used to fit machine learning algorithms.

Basin	Polygon Vertices [Longitude,Latitude; …]
Atl.	[-60,0;-100,20;-100,45;-6,45;-6,35;4,15;25,0;22,-35;-68,-35;-60,0]
Pac.*	[104,0;104,70;181,70;181,0;181,-35;145,-35;131,-30;131,0;104,0] [-180,0;-180,70;-150,70;-150,67;-120,67;-100,20;-60,0;-68,-35;-180,-35;-180,0]
Ind.	[22,-35;25,10;38,35;104,35;104,0;131,0;131,-30;116,-35;22,-35]
Arc.	[-180,64;-180,90;181,90;181,67;90,67;0,50;0,40;-6,40;-6,35;-90,35;-120,64;-180,64]
Med.	[-6.5,40;0,40;0,45;20,47;38,35;34,30;-5,30;-6.5,40]
N. Sou.	[-180,-60;-180,-25;181,-25;181,-60;-180,-60]
S. Sou.	[-180,-90;-180,-50;181,-50;181,-90;-180,-90]

*Two sets of boundaries are given for the Pacific to accommodate crossing the international date line.

Table B2. Error statistics (mean $\Delta[O_2]$ and RMSD) for tests using RFR and FNN algorithms trained on a subset of Argo and GLODAP data and tested with a separate subset of withheld data. Also shown are error statistics corresponding to the ensemble average (ENS) of the estimates from both algorithms.

Basin	Evaluation Exercise with Observational Data							
	Training Data Points	Assessment Data Points	$RFR_{Data\text{-}Eval}$		$FNN_{Data\text{-}Eval}$		$ENS_{Data\text{-}Eval}$	
			Mean $\Delta[O_2]$	RMSD	Mean $\Delta[O_2]$	RMSD	Mean $\Delta[O_2]$	RMSD
Atl.	358,316	249,549	-1.7	7.3	-1.5	7.4	-1.6	7.0
Pac.	2,318,956	534,670	-0.9	8.6	-0.2	9.3	-0.5	8.5
Ind.	550,935	275,079	-1.1	6.7	0.0	6.1	-0.5	5.6
Arc.	809,258	314,004	-2.0	8.1	-1.9	8.2	-2.0	8.0
Med.	187,296	3,316	3.9	12.0	6.2	14.0	5.0	12.4
N. Sou.	4,190,878	1,024,804	0.6	6.6	0.8	6.8	0.7	6.4
S. Sou.	4,540,439	975,698	0.3	5.6	0.1	7.0	0.2	6.0
All	12,956,078	3,377,120	-0.5	7.0	-0.2	7.6	-0.3	6.9

https://doi.org/10.5194/essd-2022-308
Preprint. Discussion started: 20 September 2022

Table B3. Error statistics (mean $\Delta[O_2]$ and RMSD) for tests using RFR and FNN algorithms trained on a subset of output from GFDL-ESM4 (corresponding to locations of available Argo and GLODAP data) and tested using a separate subset of withheld output from GDFL-ESM4. Also shown are error statistics corresponding to the ensemble average (ENS) of the estimates from both algorithms.

Basin	Evaluation Exercise with GFDL-ESM4 Output							
	Training Data Points	Assessment Data Points	$RFR_{ESM4\text{-}Eval}$		$FNN_{ESM4\text{-}Eval}$		$ENS_{ESM4\text{-}Eval}$	
			Mean $\Delta[O_2]$	RMSD	Mean $\Delta[O_2]$	RMSD	Mean $\Delta[O_2]$	RMSD
Atl.	161,122	26,720,928	-1.9	12.6	-0.3	9.6	-1.1	9.5
Pac.	473,330	65,746,512	0.3	8.7	0.0	9.7	0.2	8.5
Ind.	91,156	19,644,768	0.6	9.2	-0.4	8.7	0.1	7.8
Arc.	231,582	10,939,968	0.0	4.4	-0.1	4.7	-0.1	4.2
Med.	31,330	1,038,960	0.8	4.8	2.5	8.3	1.7	5.8
N. Sou.	701,636	64,067,328	-0.1	4.5	0.0	4.8	0.0	4.3
S. Sou.	488,176	29,759,184	0.1	3.4	-0.1	3.5	0.0	3.3
All	2,178,332	217,917,648	-0.1	8.2	-0.1	8.0	-0.1	7.2

Table B4. Error statistics (mean $\Delta[O_2]$ and RMSD) for tests using RFR and FNN algorithms trained on a subset of Argo and GLODAP data and tested with all available GLODAP data. Also shown are error statistics corresponding to the ensemble average (ENS) of the estimates from both algorithms and corresponding to the ESPER-Mixed model (Carter et al., 2021).

Basin	Evaluation Exercise with Observational Data (Tested with GLODAP Data Only)									
	Train	Test	$RFR_{Data\text{-}Eval}$		$FNN_{Data\text{-}Eval}$		$ENS_{Data\text{-}Eval}$		ESPER-Mixed	
			Mean $\Delta[O_2]$	RMSD	Mean $\Delta[O_2]$	RMSD	Mean $\Delta[O_2]$	RMSD	Mean $\Delta[O_2]$	RMSD
Atl.	358,316	59,182	0.8	7.3	1.4	11.0	1.1	8.5	-0.5	11.3
Pac.	2,318,956	189,796	0.7	7.2	0.9	11.4	0.8	8.7	-0.4	11.2
Ind.	550,935	17,211	1.6	10.0	1.1	8.6	1.3	7.8	-1.5	9.2
Arc.	809,258	68,017	0.5	7.0	0.8	10.7	0.6	8.3	1.1	12.7
Med.	187,296	48	-24.1	27.8	-32.3	39.8	-28.2	30.9	-5.2	9.6
N. Sou.	4,190,878	66,132	0.7	5.9	0.7	8.1	0.7	6.6	-0.8	8.3
S. Sou.	4,540,439	51,547	0.8	6.4	0.6	9.7	0.7	7.7	1.2	11.5
All	12,956,078	451,933	0.7	7.2	0.9	10.8	0.8	8.3	0.0	11.2

Table B5. Summary error statistics between direct observations from repeat hydrography cruises and GOBAI-O_2 and WOA18.

Cruise	GOBAI-O_2		WOA18	
	Mean $\Delta[O_2]$	RMSD	Mean $\Delta[O_2]$	RMSD
A16 (2013)	-1.4	9.6	0.2	12.0
P16 (2005)	-0.3	15.3	0.2	14.5
P02 (2012)	-1.3	10.5	-0.4	12.9
I08/I09 (2016)	-2.8	11.3	-1.1	13.0
A20 (2021)	-5.7	22.3	-2.2	21.4

https://doi.org/10.5194/essd-2022-308
Preprint. Discussion started: 20 September 2022

Open Access Earth System Science Data Discussions

Appendix C. Supplemental Text 1

Trends and associated uncertainties in GOBAI-O_2 were determined via the following procedure:

1. Spatially weighted monthly mean [O_2] values for the GOBAI-O_2 domain or within each specified depth interval were calculated from gridded [O_2], using relative grid cell volumes as weights.
2. A linear least squares model with a trend, intercept, and annual (12-month) and semi-annual (6-month) periods was fit to monthly mean [O_2] values.
3. The monthly trend from the least squares model was multiplied by 120 to obtain a **decadal trend of weighted mean [O_2]**.
4. The standard error on the trend was calculated from the covariance matrix from the least squares model.
5. The residuals from the least squares model were examined to compute the e-folding timescale, and the effective degrees of freedom were obtained by dividing the number of monthly mean [O_2] values by the e-folding timescale.
6. The standard error on the trend was scaled by the effective degrees of freedom, multiplied by 2 to obtain a 90% confidence interval, and multiplied by 120 to obtain an **uncertainty on the decadal trend of weighted mean [O_2]**.
7. The process was repeated for oxygen inventories for the GOBAI-O_2 domain or within each specified depth interval; inventories were determined from gridded [O_2], volumes of each grid cell, and densities of each grid cell.

https://doi.org/10.5194/essd-2022-308
Preprint. Discussion started: 20 September 2022

6 Data availability

GOBAI-O_2 is available as a NetCDF file at https://doi.org/10.25921/z72m-yz67 (Sharp et al., 2022; last access: 30 Aug. 2022). GLODAPv2 is updated annually and is available at www.glodap.info. GFDL-ESM4 model output can be accessed via the World Climate Research Programme database (https://esgf-node.llnl.gov/projects/cmip6/). Data from the 2018 World Ocean Atlas can be accessed through NOAA NCEI (https://www.ncei.noaa.gov/products/world-ocean-atlas). The OneArgo-Mat toolbox used to download Argo float data is available at https://doi.org/10.5281/zenodo.6588041. The toolbox acquires data from two global data assembly centers: Coriolis (ftp://ftp.ifremer.fr/ifremer/argo) and US-GODAE (ftp://usgodae.org/pub/outgoing/argo). The Roemmich and Gilson (2009) Argo-based temperature and salinity product is available at https://sio-argo.ucsd.edu/RG_Climatology.html.

7 Author contributions

JDS, AJF, BRC, and GCJ conceptualized and planned the project. JDS produced the data product, conducted all analysis, created the data visualizations, and wrote the original draft of the manuscript. JDS, AJF, BRC, GCJ, JPD, and CS reviewed and edited the manuscript.

8 Competing interests

The authors declare no competing interests.

9 Acknowledgements

The authors thank the International Argo Program and the national programs that contribute to it (https://argo.ucsd.edu, https://www.ocean-ops.org); the Argo Program is part of the Global Ocean Observing System. The authors also thank the scientists who have contributed to assembling and quality-controlling data in the GLODAP database (www.glodap.info). JDS, CS, BRC, and GCJ thank the Global Ocean Monitoring and Observing program of the National Oceanic and Atmospheric Administration (NOAA) for funding their contributions through Award NA21OAR4310251 (JDS and CS) and Project #100007298 (BRC). JDS and BRC were funded through the Cooperative Institute for Climate, Ocean, & Ecosystem Studies (CIOCES) under NOAA Cooperative Agreement NA20OAR4320271. JDS, AJF, and GCJ were supported by NOAA's Pacific Marine Environmental Laboratory (PMEL). This is CICOES contribution no. 2022-1226 and PMEL contribution no. 5416.

https://doi.org/10.5194/essd-2022-308
Preprint. Discussion started: 20 September 2022

10 References

Alkire, M. B., D'Asaro, E., Lee, C., Perry, M. J., Gray, A., Cetinić, I., Briggs, N., Rehm, E., Kallin, E., Kaiser, J., González-Posada, A. Estimates of net community production and export using high-resolution, Lagrangian measurements of O_2, NO_3^-, and POC through the evolution of a spring diatom bloom in the North Atlantic. Deep Sea Res. I 64, 157–174, https://doi.org/10.1016/j.dsr.2012.01.012, 2012.

Arteaga, L. A., Pahlow, M., Bushinsky, S. M., Sarmiento, J. L. Nutrient controls on export production in the Southern Ocean. Glob. Biogeochem. Cycl. 33, 942–956, https://doi.org/10.1029/2019GB006236, 2019.

Berman-Frank, I., Chen, Y. B., Gao, Y., Fennel, K., Follows, M. J., Milligan, A. J., Falkowski, P. G. Feedbacks between the nitrogen, carbon and oxygen cycles. In *Nitrogen in the Marine Environment*. Elsevier Inc., 1539–1563, 10.1016/B978-0-12-372522-6.00035-3, 2008.

Bianchi, D., Dunne, J. P., Sarmiento, J. L., Galbraith, E. D. Data-based estimates of suboxia, denitrification, and N_2O production in the ocean and their sensitivities to dissolved O_2. Global Biogeochemical Cycles, 26, https://doi.org/10.1029/2011GB004209, 2012.

Bindoff, N. L., Cheung, W.W.L., Kairo, J.G. et al. Changing ocean, marine ecosystems, and dependent communities. In *IPCC Special Report on the Ocean and Cryosphere in a Changing Climate*, ed. H.-O. Pörtner, C.D. Roberts, V. Masson-Delmotte, P. Zhai, E. Tignor, E. Poloczanska, K. Mintenbeck, A. Alegria, et al., 447–588, https://doi.org/10.1017/9781009157964, 2019.

Bittig, H. C., Fiedler, B., Scholz, R., Krahmann, G., Körtzinger, A. Time response of oxygen optodes on profiling platforms and its dependence on flow speed and temperature. Limnol. Oceanogr.: Methods, 12, 617–636, https://doi.org/10.4319/lom.2014.12.617, 2014.

Bittig, H. C., Körtzinger, A. Tackling oxygen optode drift: Near-surface and in-air oxygen optode measurements on a float provide an accurate in situ reference. J. Atmos. Oce. Technol., 32, 1536-1543, https://doi.org/10.1175/JTECH-D-14-00162.1, 2015.

Bittig, H. C., Körtzinger, A. Technical note: Update on response times, in-air measurements, and in situ drift for oxygen optodes on profiling platforms. Ocean Science 13, 1–11, https://doi.org/10.5194/os-13-1-2017, 2017.

Bittig, H. C., Körtzinger, A., Neill, C., van Ooijen, E., Plant, J. N., Hahn, J., Johnson, K. S., Yang, B., Emerson, S. R. Oxygen optode sensors: Principle, characterization, calibration, and application in the ocean. Front. Mar. Sci. 4, 429, https://doi.org/10.3389/fmars.2017.00429, 2018a.

Bittig, H. C., Steinhoff, T., Claustre, H., Fiedler, B., Williams, N. L., Sauzède, R., Körtzinger, A., Gattuso, J. P. An alternative to static climatologies: Robust estimation of open ocean CO_2 variables and nutrient concentrations from T, S, and O_2 data using Bayesian neural networks. Front. Mar. Sci. 5, 328, https://doi.org/10.3389/fmars.2018.00328, 2018b.

Bittig, H., Wong, A., Plant, J. BGC-Argo synthetic profile file processing and format on Coriolis GDAC. Ifremer, Plouzane, France, https://doi.org/10.13155/55637, 2022.

Bopp, L., Resplandy, L., Orr, J. C., Doney, S. C., Dunne, J. P., Gehlen, M., Halloran, P., Heinze, C., Ilyina, T., Séférian, R., Tjiputra, J., Vichi, M. Multiple stressors of ocean ecosystems in the 21st century: Projections with CMIP5 models. Biogeosciences 10, 6225–6245, https://doi.org/10.5194/bg-10-6225-2013, 2013.

Boyer, T. P., Baranova, O. K., Coleman, C., Garcia, H. E., Grodsky, A., Locarnini, R. A., Mishonov, A. V., Paver, C. R., Reagan, J. R., Seidov, D., Smolyar, I. V., Weathers, K., Zweng, M. M. World Ocean Database 2018. A.V. Mishonov, Technical Ed., NOAA Atlas NESDIS 87, 2018.

Breiman, L. Random forests, Mach. Learn., 45, 5–32, https://doi.org/10.1023/A:1010933404324, 2001.

Breitburg, D., Levin, L. A., Oschlies, A., Grégoire, M., Chavez, F. P., Conley, D. J., ... Zhang, J. Declining oxygen in the global ocean and coastal waters. Science, 359, 10.1126/science.aam7240, 2018.

Bushinsky, S. M., Emerson, S. Marine biological production from in situ oxygen measurements on a profiling float in the subarctic Pacific Ocean. Glob. Biogeochem. Cycl. 29, 2050–2060, https://doi.org/10.1002/2015GB005251, 2015.

Bushinsky, S. M., Emerson, S. R., Riser, S. C., Swift, D. D. Accurate oxygen measurements on modified Argo floats using in situ air calibrations. Limnol. Oceanogr.: Methods 14, 491–505, https://doi.org/10.1002/lom3.10107, 2016.

Bushinsky, S. M., Gray, A. R., Johnson, K. S., Sarmiento, J. L. Oxygen in the Southern Ocean from Argo floats: Determination of processes driving air-sea fluxes. JGR: Oceans, 122, 8661–8682, https://doi.org/10.1002/2017JC012923, 2017.

Bushinsky, S. M., Emerson, S. R. Biological and physical controls on the oxygen cycle in the Kuroshio Extension from an array of profiling floats. Deep Sea Res. I, 141, 51–70, https://doi.org/10.1016/j.dsr.2018.09.005, 2018.

Carpenter, J. H. The Chesapeake Bay Institute technique for the Winkler dissolved oxygen method. Limnol. Oceanogr. 10, 141–143, 1965.

Carter, B. R., Bittig, H. C., Fassbender, A. J., Sharp, J. D., Takeshita, Y., Xu, Y. Y., Álvarez, M., Wanninkhof, R., Feely, R. A., Barbero, L. New and updated global empirical seawater property estimation routines. Limnol. Oceanogr.: Methods 19, 785–809, https://doi.org/10.1002/lom3.10461, 2021.

Chierici, M., Fransson, A., Turner, D. R., Pakhomov, E. A., Froneman, P. W. Variability in pH, fCO2, oxygen and flux of CO2 in the surface water along a transect in the Atlantic sector of the Southern Ocean. Deep Sea Res. II 51, 2773–2787, https://doi.org/10.1016/j.dsr2.2001.03.002, 2004.

Claustre, H., Johnson, K. S., Takeshita, Y. Observing the global ocean with biogeochemical-Argo. Annual Rev. Mar. Sci., 12, 23–48, 10.1146/annurev-marine-010419-010956, 2020.

D'Asaro, E. A., McNeil, C. Calibration and stability of oxygen sensors on autonomous floats. J. of Atmosph. Oceanic Technol. 30, 1896–1906, https://doi.org/10.1175/JTECH-D-12-00222.1, 2013.

Demuth, H., Beale, M., Hagan, M.: Neural Network Toolbox 6 User's Guide, The MathWorks, Inc., 3 Apple Hill Drive, Natick, MA, 2008.

Djeutchouang, L. M., Chang, N., Gregor, L., Vichi, M., Monteiro, P. M. S. The sensitivity of pCO2 reconstructions in the Southern Ocean to sampling scales: a semi-idealized model sampling and reconstruction approach. Biogeosciences Discussions 1–36, https://doi.org/10.5194/bg-2021-344, 2022.

Drucker, R., Riser, S. C. In situ phase-domain calibration of oxygen Optodes on profiling floats. Methods in Oceanography 17, 296–318. https://doi.org/10.1016/j.mio.2016.09.007, 2016.

Dunne, J. P., Horowitz, L. W., Adcroft, A. J., Ginoux, P., Held, I. M., John, J. G., ... Zhao, M. The GFDL Earth System Model version 4.1 (GFDL-ESM 4.1): Overall coupled model description and simulation characteristics. J. Adv. Modeling Earth Syst. 12, e2019MS002015, https://doi.org/10.1029/2019MS002015, 2020.

Estapa M. L., Feen M. L., Breves E. Direct observations of biological carbon export from profiling floats in the subtropical North Atlantic. Glob. Biogeochem. Cycles 33, 282–300, https://doi.org/10.1029/2018GB006098, 2019.

Fay, A. R., McKinley, G. A. Global open-ocean biomes: mean and temporal variability. Earth Syst. Sci. Data 6, 273–284, https://doi.org/10.5194/essd-6-273-2014, 2014.

Fiedler, B., Fietzek, P., Vieira, N., Silva, P., Bittig, H. C., Körtzinger, A. In Situ CO_2 and O_2 Measurements on a Profiling Float. J. Atmos. Ocean. Tech. 30, 112–126, https://doi.org/10.1175/JTECH-D-12-00043.1, 2013.

Frenzel, H., Sharp, J. D., Fassbender, A. J., Buzby, N. OneArgo-Mat: A MATLAB toolbox for accessing and visualizing Argo data (v1.0.2), Zenodo, https://doi.org/10.5281/zenodo.6588041, 2022.

Frölicher, T. L., Joos, F., Plattner, G. K., Steinacher, M., Doney, S. C. Natural variability and anthropogenic trends in oceanic oxygen in a coupled carbon cycle–climate model ensemble. Global Biogeochemical Cycles 23, https://doi.org/10.1029/2008GB003316, 2009.

Garcia, H. E., Gordon, L. I. Oxygen solubility in seawater: Better fitting equations. Limnol. Oceanogr., 37, 1307–1312, https://doi.org/10.4319/lo.1992.37.6.1307, 1992.

Garcia, H. E., Weathers, K. W., Paver, C. R., Smolyar, I., Boyer, T. P., Locarnini, M. M., ... Seidov, D. World Ocean Atlas 2018, Volume 3: Dissolved Oxygen, Apparent Oxygen Utilization, and Dissolved Oxygen Saturation, NOAA Atlas NESDIS 83, https://archimer.ifremer.fr/doc/00651/76337, 2019.

Garcia-Soto, C., Cheng, L., Caesar, L., Schmidtko, S., Jewett, E. B., Cheripka, A., Rigor, I., Caballero, A., Chiba, S., Báez, J. C., Zielinski, T., Abraham, J. P. An Overview of Ocean Climate Change Indicators: Sea Surface Temperature, Ocean Heat Content, Ocean pH, Dissolved Oxygen Concentration, Arctic Sea Ice Extent, Thickness and Volume, Sea Level and Strength of the AMOC (Atlantic Meridional Overturning Circulation). Front. Mar. Sci. 8, 642372, https://doi.org/10.3389/fmars.2021.642372, 2021.

Giglio, D., Lyubchich, V., Mazloff, M. R. Estimating oxygen in the Southern Ocean using Argo temperature and salinity. JGR: Oceans, 123, 4280–4297, https://doi.org/10.1029/2017JC013404, 2018.

Gregor, L., Kok, S., Monteiro, P. M. S. Empirical methods for the estimation of Southern Ocean CO_2: Support Vector and Random Forest Regression. Biogeosciences, 14, 5551–5569, https://doi.org/10.5194/bg-14-5551-2017, 2017.

Gregor, L., Lebehot, A. D., Kok, S., Monteiro, P. M. S. A comparative assessment of the uncertainties of global surface ocean CO2 estimates using a machine-learning ensemble (CSIR-ML6 version 2019a) – Have we hit the wall? Geosci. Model Dev., 12, 5113–5136. https://doi.org/10.5194/gmd-12-5113-2019, 2019.

Grégoire, M., Garçon, V., Garcia, H., Breitburg, D., Isensee, K., Oschlies, A., Telszewski, M., Barth, A., Bittig, H.C., Carstensen, J., Carval, T., Chai, F., Chavez, F., Conley, D., Coppola, L., Crowe, S., Currie, K., Dai, M., Deflandre, B., Dewitte, B., Diaz, R., Garcia-Robledo, E., Gilbert, D., Giorgetti, A., Glud, R., Gutierrez, D., Hosoda, S., Ishii, M., Jacinto, G., Langdon, C., Lauvset, S.K., Levin, L. A., Limburg, K. E., Mehrtens, H., Montes, I., Naqvi, W., Paulmier, A., Pfeil, B., Pitcher, G., Pouliquen, S., Rabalais, N., Rabouille, C., Recape, V., Roman, M., Rose, K., Rudnick, D., Rummer, J., Schmechtig, C., Schmidtko, S., Seibel, B., Slomp, C., Sumalia, U. R., Tanhua, T., Thierry, V., Uchida, H., Wanninkhof, R.,

Yasuhara, M. A Global Ocean Oxygen Database and Atlas for Assessing and Predicting Deoxygenation and Ocean Health in the Open and Coastal Ocean. Front. Mar. Sci. 8, 724913. https://doi.org/10.3389/fmars.2021.724913, 2021.

Gregor, L., Gruber, N. OceanSODA-ETHZ: a global gridded data set of the surface ocean carbonate system for seasonal to decadal studies of ocean acidification. Earth Syst. Sci. Data, 13, 777–808, https://doi.org/10.5194/essd-13-777-2021, 2021.

Gruber, N., Gloor, M., Fan, S.-M., Sarmiento, J. L. Air-sea flux of oxygen estimated from bulk data: Implications For the marine and atmospheric oxygen cycles. Glob. Biogeochem. Cycl., 15, 783–803, https://doi.org/10.1029/2000GB001302, 2001.

Gruber, N. The dynamics of the marine nitrogen cycle and its influence on atmospheric CO_2 variations. In The ocean carbon cycle and climate. Springer, Dordrecht, 97–148, 2004.

Gruber, N., Doney, S., Emerson, S., Gilbert, D., Kobayashi, T., Körtzinger, A., Johnson, G., Johnson, K., Riser, S., and Ulloa, O.: Adding oxygen to Argo: Developing a global in-situ observatory for ocean deoxygenation and biogeochemistry. In: Proceedings of OceanObs'09: Sustained Ocean Observations and Information for Society, Venice, Italy, 21–25 September 2009, ESA Publication WPP-306, Eds.: Hall, J., Harrison, D., and Stammer, D., https://doi.org/10.5270/OceanObs09.cwp.39, 2010.

Helm, K. P., Bindoff, N. L., Church, J. A. Observed decreases in oxygen content of the global ocean. Geophys. Res. Lett. 38, 1–6, https://doi.org/10.1029/2011GL049513, 2011.

Ito, T., Minobe, S., Long, M. C., Deutsch, C. Upper ocean O_2 trends: 1958–2015. Geophysical Research Letters 44, 4214–4223, https://doi.org/10.1002/2017GL073613, 2017.

Johnson, K. S., Plant, J. N., Riser, S. C., Gilbert, D. Air oxygen calibration of oxygen optodes on a profiling float array. J. Atmos. Oceanic Technol. 32, 2160–2172, https://doi.org/10.1175/JTECH-D-15-0101.1, 2015.

Johnson, K., Claustre, H. Bringing biogeochemistry into the Argo age. Eos 97, https://doi.org/10.1029/2016EO062427, 2016.

Johnson, K. S., Plant, J. N., Coletti, L. J., Jannasch, H. W., Sakamoto, C. M., Riser, S. C., Swift, D. D., Williams, N. L., Boss, E., Haëntjens, N., Talley, L. D., Sarmiento, J. L. Biogeochemical sensor performance in the SOCCOM profiling float array. JGR: Oceans, 122, 6416–6436. https://doi.org/10.1002/2017JC012838, 2017.

Johnson, K. S., Riser, S. C., Ravichandran, M. Oxygen variability controls denitrification in the Bay of Bengal oxygen minimum zone. Geophys. Res. Lett., 46, 804–811, https://doi.org/10.1029/2018GL079881, 2019.

Johnson, K. S., Bif, M. B. Constraint on net primary productivity of the global ocean by Argo oxygen measurements. Nature Geoscience, 14, 769–774, https://doi.org/10.1038/s41561-021-00807-z, 2021.

Jonsson, B. F., Doney, S. C., Dunne, J., Bender, M. Evaluation of the Southern Ocean O_2/Ar-based NCP estimates in a model framework. Journal of Geophysical Research: Biogeosciences, 118, 385–399, https://doi.org/10.1002/jgrg.20032, 2013.

Keeling, R. F., Arne, K., Gruber, N. Ocean Deoxygenation in a Warming World. Ann. Rev. Mar Sci. 2, 199–229, https://doi.org/10.1146/annurev.marine.010908.163855, 2010.

Keppler, L., Landschützer, P., Gruber, N., Lauvset, S. K., Stemmler, I. Seasonal carbon dynamics in the near-global ocean. Glob. Biogeochem. Cycl., 34, e2020GB006571, https://doi.org/10.1029/2020GB006571, 2020.

Körtzinger A., Schimanski J., Send U., Wallace D. The ocean takes a deep breath. Science 306, 1337, https://doi.org/10.1126/science.1102557, 2004.

Körtzinger, A., Schimanski, J., Send, U. High Quality Oxygen Measurements from Profiling Floats: A Promising New Technique, J. Atmos. Ocean. Tech., 22, 302–308, doi:10.1175/JTECH1701.1, 2005.

Kwiatkowski, L., Torres, O., Bopp, L., Aumont, O., Chamberlain, M., Christian, J., Dunne, J., Gehlen, M., Ilyina, T., John, J., Lenton, A., Li, H., Lovenduski, N., Orr, J., Palmieri, J., Schwinger, J., Séférian, R., Stock, C., Tagliabue, A., Takano, Y., Tjiputra, J., Toyama, K., Tsujino, H., Watanabe, M., Yamamoto, A., Yool, A., Ziehn, T. Twenty-first century ocean warming, acidification, deoxygenation, and upper ocean nutrient decline from CMIP6 model projections. Biogeosciences 17, 3439–3470, https://doi.org/10.5194/bg-2020-16, 2020.

Landschützer, P., Gruber, N., Bakker, D. C. E., Schuster, U. Recent variability of the global ocean carbon sink. Global Biogeochem. Cycles, 28, 927–949, https://doi.org/10.1002/2014GB004853, 2014.

Langdon, C. Determination of Dissolved Oxygen in Seaweater By Winkler Titration using Amperometric Technique. In *The GO-SHIP Repeat Hydrography Manual: A Collection of Expert Reports and Guidelines*. Version 1, (eds. Hood, E.M., C.L. Sabine, and B.M. Sloyan). 18pp. (IOCCP Report Number 14; ICPO Publication Series Number 134). https://doi.org/10.25607/OBP-1350, 2010.

Lauvset, S. K., Lange, N., Tanhua, T., Bittig, H. C., Olsen, A., Kozyr, A., Álvarez, M. Becker, S. Brown, P. J., Carter, B. R., Cotrim da Cunha, L., Feely, R. A., van Heuven, S., Hoppema, M., Ishii, M., Jeansson, E., Jutterström, S., Jones, S. D., Karlsen, M. K., Lo Monaco, C., Michaelis, P., Murata, A., Pérez, F. F., Pfeil, B., Schirnick, C., Steinfeldt, R., Suzuki, T., Tilbrook, B., Velo, A., Wanninkhof, R., Woosley, R. J., Key, R.M. An updated version of the global interior ocean biogeochemical data product, GLODAPv2.2021. Earth Syst. Sci. Data, 13, 5565–5589, https://doi.org/10.5194/essd-13-5565-2021, 2021.

Limburg, K. E., Breitburg, D., Swaney, D. P., Jacinto, G. Ocean deoxygenation: A primer. One Earth, 2, 24–29, https://doi.org/10.1016/j.oneear.2020.01.001, 2020.

Maurer, T. L., Plant, J. N., Johnson, K. S. Delayed-Mode Quality Control of Oxygen, Nitrate, and pH Data on SOCCOM Biogeochemical Profiling Floats. Front. Mar. Sci., 8, https://doi.org/10.3389/fmars.2021.683207, 2021.

McDougall, T. J., Barker, P. M. Getting started with TEOS-10 and the Gibbs Seawater (GSW) oceanographic toolbox. Scor/Iapso WG, 127, 1–28, 2011.

Nicholson, D. P., & Feen, M. L. Air calibration of an oxygen optode on an underwater glider. Limnol. Oceanogr.: Methods, 15, 495–502. https://doi.org/10.1002/lom3.10177, 2017.

NOAA National Geophysical Data Center. 2-minute Gridded Global Relief Data (ETOPO2) v2. NOAA National Centers for Environmental Information. https://doi.org/10.7289/V5J1012Q. 2006. Accessed 7/30/2021.

Oschlies, A., Duteil, O., Getzlaff, J., Koeve, W., Landolfi, A., Schmidtko, S. Patterns of deoxygenation: sensitivity to natural and anthropogenic drivers. Phil Trans. Royal Soc. A, 375, 20160325, https://doi.org/10.1098/rsta.2016.0325, 2017.

Oschlies, A., Brandt, P., Stramma, L., Schmidtko, S. Drivers and mechanisms of ocean deoxygenation. Nature Geoscience, 11, 467–473. https://doi.org/10.1038/s41561-018-0152-2, 2018.

Piron, A., Thierry, V., Mercier, H., Caniaux, G. Argo float observations of basin-scale deep convection in the Irminger sea during winter 2011–2012. Deep Sea Res. I, 109, 76–90, https://doi.org/10.1016/j.dsr.2015.12.012, 2016.

Piron, A., Thierry, V., Mercier, H., and Caniaux, G. Gyre-scale deep convection in the subpolar North Atlantic Ocean during winter 2014–2015. Geophys. Res. Lett., 44, 1439–1447, https://doi.org/10.1002/2016GL071895, 2017.

Pörtner, H. O., Farrell, A. P. Physiology and climate change. Science, 322, 690–692, https://doi.org/10.1126/science.1163156, 2008.

Reuer, M. K., Barnett, B. A., Bender, M. L., Falkowski, P. G., Hendricks, M. B. New estimates of Southern Ocean biological production rates from O_2/Ar ratios and the triple isotope composition of O_2. Deep Sea Res. I, 54, 951–974, https://doi.org/10.1016/j.dsr.2007.02.007, 2007.

Ritter, R., Landschützer, P., Gruber, N., Fay, A. R., Iida, Y., Jones, S., Zeng, J. Observation-Based Trends of the Southern Ocean Carbon Sink, Geophys. Res. Lett., 2, 339–348, https://doi.org/10.1002/2017GL074837, 2017.

Roemmich, D., Gilson, J. The 2004-2008 mean and annual cycle of temperature, salinity, and steric height in the global ocean from the Argo Program. Progress in Oceanography, 82, 81–100. https://doi.org/10.1016/j.pocean.2009.03.004, 2009.

Roemmich, D., Alford, M. H., Claustre, H., Johnson, K. S., et al. On the future of Argo: A global, full-depth, multi-disciplinary array. Frontiers in Marine Science, 6, 1–28. https://doi.org/10.3389/fmars.2019.00439, 2019.

Roemmich, D., L. Talley, N. Zilberman, E. Osborne, K.S. Johnson, L. Barbero, H.C. Bittig, N. Briggs, A.J. Fassbender, G.C. Johnson, B.A. King, E. McDonagh, S. Purkey, S. Riser, T. Suga, Y. Takeshita, V. Thierry, and S. Wijffels. The technological, scientific, and sociological revolution of global subsurface ocean observing. In *Frontiers in Ocean Observing: Documenting Ecosystems, Understanding Environmental Changes, Forecasting Hazards*. Eds. E.S. Kappel, S.K. Juniper, S. Seeyave, E. Smith, M. Visbeck, 2–8. A Supplement to Oceanography 34, https://doi.org/10.5670/oceanog.2021.supplement.02-02, 2021.

Sampaio, E., Santos, C., Rosa, I. C., Ferreira, V., Pörtner, H., Duarte, C. M., et al. Impacts of hypoxic events surpass those of future ocean warming and acidification. Nature Ecology & Evolution, 5, 311–321. https://doi.org/10.1038/s41559-020-01370-3, 2021.

Sauzède, R., Claustre, H., Jamet, C., Uitz, J., Ras, J., Mignot, A., d'Ortenzio, F. Retrieving the vertical distribution of chlorophyll a concentration and phytoplankton community composition from in situ fluorescence profiles: A method based on a neural network with potential for global-scale applications. JGR: Oceans, 120, 451–470, https://doi.org/10.1002/2014JC010355, 2015.

Sauzède, R., Claustre, H., Uitz, J., Jamet, C., Dall'Olmo, G., d'Ortenzio, F., Gentili, B., Poteau, A., Schmechtig, C. A neural network based method for merging ocean color and Argo data to extend surface bio optical properties to depth: Retrieval of the particulate backscattering coefficient. JGR: Oceans, 121, 2552–2571, https://doi.org/10.1002/2015JC011408, 2016.

Sauzède, R., Claustre, H., Pannimpullath, R., Uitz, J., Guinehut, S. New Global Vertical Distribution of Gridded Particulate Organic Carbon and Chlorophyll Concentration Using Machine Learning for CMEMs. In 9th EuroGOOS International conference, https://hal.archives-ouvertes.fr/hal-03335370, 2021.

Sarma V. V. S. S., Udaya Bhaskar T. V. S. Ventilation of oxygen to oxygen minimum zone due to anticyclonic eddies in the Bay of Bengal. J. Geophys. Res. Biogeosci. 123, 2145–2153, https://doi.org/10.1029/2018JG004447, 2018.

Sarmiento, J.L., Gruber, N. Ocean Biogeochemical Dynamics. Princeton University Press, Princeton, NJ, 2006.

Schofield, O., A. Fassbender, M. Hood, K. Hill, K. Johnson. A global ocean biogeochemical observatory becomes a reality, Eos, 103, https://doi.org/10.1029/2022EO220149, 2022.

Schmidtko, S., Stramma, L., Visbeck, M. Decline in global oceanic oxygen content during the past five decades. Nature, 542, https://doi.org/10.1038/nature21399, 335–339, 2017.

Sharp, J. D., Fassbender, A. J., Carter, B. R., Johnson, G. C., Schultz, C., Dunne, J. P. GOBAI-O2: A Global Gridded Monthly Dataset of Ocean Interior Dissolved Oxygen Concentrations Based on Shipboard and Autonomous Observations (NCEI Accession 0259304). v1.0. NOAA National Centers for Environmental Information. Dataset. https://doi.org/10.25921/z72m-yz67

Stramma, L., Schmidtko, S. Global evidence of ocean deoxygenation. In Ocean Deoxygenation: Everyone's Problem. Eds. D. Laffoley, J. M. Baxter. 25-26. IUCN. Gland, Switzerland, 2019.

Stukel MR, Ducklow HW. Stirring up the biological pump: vertical mixing and carbon export in the Southern Ocean. Glob. Biogeochem. Cycles 31, 1420–1434, https://doi.org/10.1002/2017GB005652, 2017.

Takeshita, Y., Martz, T. R., Johnson, K. S., Plant, J. N., Gilbert, D., Riser, S. C., Neill, C., Tilbrook, B. A climatology-based quality control procedure for profiling float oxygen data. JGR: Oceans, 118, 5640–5650. https://doi.org/10.1002/jgrc.20399, 2013.

Talley, L. D. Descriptive physical oceanography: an introduction. Academic press, 2011.

Testor, P., de Young, B., Rudnick, D. L., Glenn, S., Hayes, D., Lee, C. L., et al. OceanGliders: A component of the integrated GOOS. Front. Mar. Sci. 6, 422, 10.3389/fmars.2019.00422, 2019.

Udaya Bhaskar, T. V. S., Sarma, V. V. S. S., Pavan Kumar, J. Potential mechanisms responsible for spatial variability in intensity and thickness of oxygen minimum zone in the Bay of Bengal. JGR: Biogeosciences 126, https://doi.org/10.1029/2021JG006341, 2021.

Winkler, L. W. Die Bestimmung des imWasser gelösten Sauerstoffes. Chem. Ber. 21, 2843–2855. 10.1002/cber.188802102122, 1888.

Wolf M. K., Hamme R. C., Gilbert D., Yashayaev I., Thierry V. Oxygen saturation surrounding deep water formation events in the Labrador Sea from Argo-O_2 data. Glob. Biogeochem. Cycles 32, 635–653, https://doi.org/10.1002/2017GB005829, 2018.

Yang, B., Emerson, S. R., and Bushinsky, S. M. Annual net community production in the subtropical Pacific Ocean from in situ oxygen measurements on profiling floats. Glob. Biogeochem. Cycl. 31, 728–744, https://doi.org/10.1002/2016GB005545, 2017.